Article

Cell Reports

Unveiling IRF4-steered regulation of context-dependent effector programs in CD4⁺ T cells under Th17- and Treg-skewing conditions

Graphical abstract

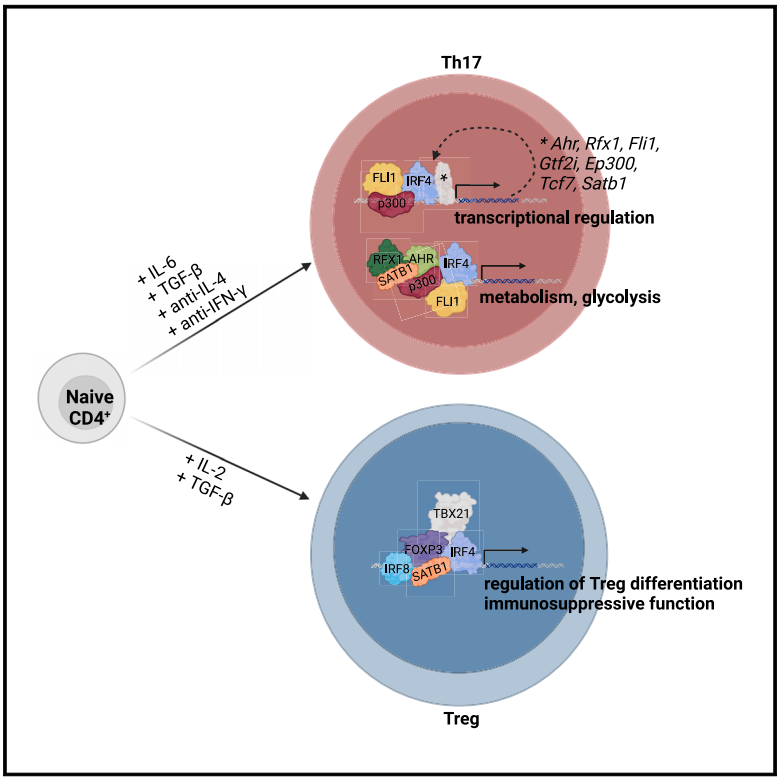

Highlights

- Comprehensive characterization of IRF4-mediated regulatory programs in Th17 and iTreg cells
- Co-recruitment of IRF4 interactors to composite elements
- FLI1 is a key IRF4 partner in Th17 function regulation

Authors

Anna Gabele, Maximilian Sprang, Mert Cihan, ..., Katja Luck, Tobias Bopp, Ute Distler

Correspondence

boppt@uni-mainz.de (T.B.), ute.distler@uni-mainz.de (U.D.)

In brief

Gabele et al. performed an integrated analysis of IRF4-mediated gene regulation in Th17 and iTreg cells, utilizing ChIP-seq, interactome, and proteome data. This enabled the identification of IRF4 interactors that are recruited together with IRF4 to composite elements, including FLI1, which promotes, in cooperation with IRF4, Th17 transcriptional programs.

Gabele et al., 2025, Cell Reports *44*, 115407
March 25, 2025
https://doi.org/10.1016/j.celrep.2025.115407

CellPress

Cell Reports

CellPress
OPEN ACCESS

Article

Unveiling IRF4-steered regulation of context-dependent effector programs in CD4+ T cells under Th17- and Treg-skewing conditions

Anna Gabele,[1,2,13] Maximilian Sprang,[3,13] Mert Cihan,[3] Mareen Welzel,[4] Assel Nurbekova,[1] Karolina Romaniuk,[1] Sarah Dietzen,[1,2,5] Matthias Klein,[1,2] Georg Bündgen,[1] Maxim Emelianov,[1] Gregory Harms,[2,6] Krishnaraj Rajalingam,[2,6] Tanja Ziesmann,[1] Katrin Pape,[7] Beatrice Wasser,[7] David Gomez-Zepeda,[8,9] Kathrin Braband,[1] Michael Delacher,[1,2] Niels Lemmermann,[2,10,11] Stefan Bittner,[2,7,12] Miguel A. Andrade-Navarro,[3] Stefan Tenzer,[1,2,8,9] Katja Luck,[4] Tobias Bopp,[1,2,*] and Ute Distler[1,2,14,*]

[1]Institute of Immunology, University Medical Center of the Johannes Gutenberg University Mainz, 55131 Mainz, Germany
[2]Research Center for Immunotherapy, University Medical Center of the Johannes Gutenberg University Mainz, 55131 Mainz, Germany
[3]Faculty of Biology, Johannes Gutenberg University Mainz, 55128 Mainz, Germany
[4]Institute of Molecular Biology gGmbH, 55128 Mainz, Germany
[5]Novo Nordisk Pharma GmbH, 55124 Mainz, Germany
[6]Cell Biology Unit, University Medical Center of the Johannes Gutenberg University Mainz, 55131 Mainz, Germany
[7]Department of Neurology, University Medical Center of the Johannes Gutenberg University Mainz, 55131 Mainz, Germany
[8]Helmholtz Institute for Translational Oncology, 55131 Mainz, Germany
[9]Deutsches Krebsforschungszentrum, 69120 Heidelberg, Germany
[10]Institute for Virology, University Medical Center of the Johannes Gutenberg University Mainz, 55131 Mainz, Germany
[11]Institute of Virology, Medical Faculty, University Bonn, 53127 Bonn, Germany
[12]Focus Program Translational Neuroscience, University Medical Center of the Johannes Gutenberg University Mainz, 55131 Mainz, Germany
[13]These authors contributed equally
[14]Lead contact
*Correspondence: boppt@uni-mainz.de (T.B.), ute.distler@uni-mainz.de (U.D.)
https://doi.org/10.1016/j.celrep.2025.115407

SUMMARY

The transcription factor interferon regulatory factor 4 (IRF4) is crucial for the fate determination of pro-inflammatory T helper (Th) 17 and the functionally opposing group of immunomodulatory regulatory T (Treg) cells. However, the molecular mechanisms of how IRF4 steers diverse transcriptional programs in Th17 and Treg cells are far from being definitive. Here, we integrated data derived from affinity-purification and full mass-spectrometry-based proteome analysis with chromatin immunoprecipitation sequencing. This allowed the characterization of subtype-specific molecular programs and the identification of IRF4 interactors in the Th17/Treg context. Our data reveal that IRF4-interacting transcription factors are recruited to IRF composite elements for the regulation of cell-type-specific transcriptional programs as exemplarily demonstrated for FLI1, which, in cooperation with IRF4, promotes Th17-specific gene expression. FLI1 inhibition markedly impaired Th17 differentiation. The present "omics" dataset provides a valuable resource for studying IRF4-mediated gene regulatory programs in pro- and anti-inflammatory immune responses.

INTRODUCTION

The transcription factor (TF) interferon regulatory factor 4 (IRF4) is one of nine members of the mammalian family of interferon regulatory factors (IRFs), which steer different aspects of innate and adaptive immune responses.[1,2] IRF4 expression is restricted to immune cells. As IRF4 acts as one of the key regulators in the differentiation of T and B cells, dysregulation of IRF4 is often associated with diseases like cancer and autoimmune disorders such as multiple sclerosis. Pro-inflammatory T helper (Th) 17 cells, which have been implicated in the initiation and progression of autoimmune diseases, heavily rely on the expression of IRF4 during their development.[2] Regulatory T (Treg) cells, which contribute to the maintenance of peripheral tolerance by preventing autoaggressive immune responses, do not directly rely on IRF4 for their generation.[3] However, IRF4 is essential for the context- and tissue-specific effector functions of this T cell type.[1,3,4]

Numerous studies have focused on elucidating the molecular mechanisms of IRF4-mediated gene expression essential for murine and human Th17 and Treg cell lineage determination, demonstrating direct IRF4 binding to key lineage-associated loci in Th17 cells.[5,6] Lack of IRF4 results in decreased expression of RORγt, the lineage-defining TF for Th17 cells.[2] In Treg cells, IRF4, in concert with BATF3, regulates the expression of the lineage-specific TF FOXP3 and hence controls iTreg induction.[7]

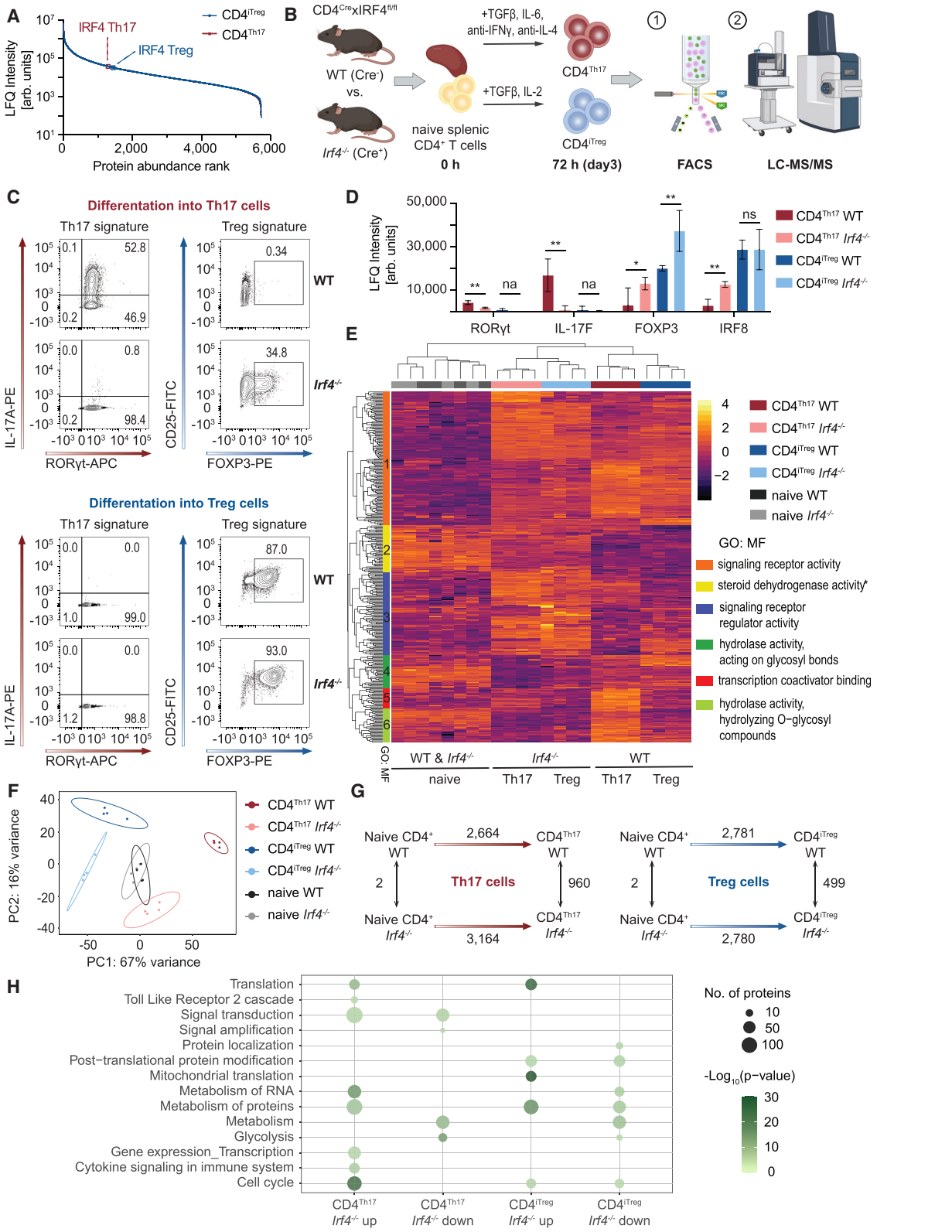

(legend on next page)

Despite its repressive function on FOXP3 expression, IRF4 acts as a downstream target of FOXP3 and is required for the development of fully functional Treg cells and their immunomodulatory activity in a cellular context.[4,7] In a complex, IRF4 and FOXP3 control the expression of gene loci associated with Treg cell suppressive properties, e.g., *Il10* and *Icos*.[8,9] Moreover, IRF4 directly controls a molecular program associated with increased immunosuppression in human tumors.[10] Although respective studies have identified IRF4-mediated transcriptional programs in Th17 and Treg cells, certain underlying molecular mechanisms are still not fully understood. The majority of the studies focuses mainly on the target genes transcribed by IRF4, often at early time points during cellular differentiation (e.g., after 48 h).[5,7,11] However, gene expression is controlled by multiple molecular systems, but only a very limited number of studies so far have integrated information derived from IRF4 chromatin immunoprecipitation sequencing (ChIP-seq) data with other "omics" data at a global level in an unbiased manner (e.g., with transcriptomics[5] or proteomics analysis) or elucidated proteins that regulate gene transcription in concert with IRF4 in a T cell subset-specific manner. Here, our current knowledge is mainly set on a few distinct binding partners,[6,8,9,12] and it remains unresolved how IRF4-interacting proteins steer IRF4-mediated target gene transcription contributing to the cellular plasticity between Treg and Th17 cells.[3]

Affinity purification (AP) methods, such as the streptavidin capture of biotinylated proteins, coupled with mass spectrometry (MS) enable the comprehensive characterization of protein-protein interactions (PPIs).[13] In 2005, Driegen et al. introduced a transgenic mouse strain ubiquitously expressing the bacterial BirA protein biotin ligase from the ROSA26 locus (ROSA26^{BirA} mice),[14] which biotinylates a short peptide sequence, termed Avi-tag. Crossing ROSA26^{BirA} mice with transgenic mice expressing Avi-tagged proteins efficiently biotinylates the protein of interest for the purpose of protein (complex) purification. Beside the characterization of PPIs, this approach also enables the identification of target genes regulated by the TF (complex) of interest by applying streptavidin-mediated chromatin precipitation coupled with deep sequencing (Bio-ChIP-seq).[15] In the present study, we integrate AP-MS and Bio-ChIP-seq with MS-based proteome analyses to reveal IRF4-driven lineage determination in Treg and Th17 cells. Our data unraveled a complex and T cell subset-specific network of IRF-steered transcriptional regulation of T cell differentiation and plasticity.

RESULTS

IRF4 transcriptionally regulates distinct effector functions in Th17 and Treg cells

Comparative analyses of Th17 and Treg cells revealed that IRF4 is expressed at similar protein levels in both cell types (Figure 1A). To better understand the role of IRF4 in cellular plasticity in Th17 and Treg cells, we analyzed the full proteome of both cell types after *ex vivo* differentiation of naive CD4$^+$ T cells derived from conditional IRF4-deficient (*Irf4*$^{-/-}$) and littermate control (wild-type [WT]) mice. To this end, CD4$^+$ T cells were stimulated for 72 h under Th17- (CD4^{Th17}) or induced (i)Treg-skewing (CD4^{iTreg}) conditions (Figure 1B).

In line with previous data,[2] proteomic as well as flow cytometry-based analysis confirmed that interleukin (IL)-17-secreting CD4^{Th17} cells cannot develop in the absence of IRF4 (Figures 1C and 1D). Concomitant with strongly reduced IL-17 production, IRF4-deficient CD4^{Th17} cells displayed significantly reduced expression of RORγt (Figure 1D). In contrast, development of *in vitro*-induced FOXP3$^+$ CD4^{iTreg} cells from *Irf4*$^{-/-}$ naive T cells was not affected. Interestingly, *Irf4*$^{-/-}$ CD4^{iTreg} cells showed significantly increased FOXP3 levels as compared to CD4^{iTreg} cells differentiated from WT mice, confirming the repressive effect of IRF4 on FOXP3 expression (Figures 1C and 1D). However, in-depth proteomic analysis revealed that *Irf4*$^{-/-}$ CD4^{iTreg} cells still differ markedly from WT CD4^{iTreg} cells regarding their protein expression pattern (see Figures 1E and 1F). Principal-component analysis (PCA) of protein abundances demonstrated substantial differences between IRF4-deficient and IRF4-competent cells (Figure 1F). While principal component 1 (PC1) reflects major changes between fully differentiated CD4^{Th17} and CD4^{iTreg} cells, PC2 additionally separated *Irf4*$^{-/-}$ cells from their WT counterparts, indicating a stronger divergence for *Irf4*$^{-/-}$ CD4^{Th17} cells as compared to *Irf4*$^{-/-}$ CD4^{iTreg} cells. This is also reflected in the overall number of differentially expressed proteins: upon differentiation from naive CD4$^+$

Figure 1. Proteomic analysis of CD4^{Th17} and CD4^{iTreg} cells from *Irf4*$^{-/-}$ and littermate control (WT) mice reveals marked changes in pathways required for cellular effector functions

Naive splenic CD4$^+$ T cells of *Irf4*$^{-/-}$ and littermate controls were stimulated for 72 h under Th17- (CD4^{Th17}) and iTreg-polarizing (CD4^{iTreg}) conditions and subsequently analyzed by label-free quantitative MS (n = 4).

(A) IRF4 expression levels in CD4^{Th17} and CD4^{iTreg} cells from WT mice.

(B) Experimental setup for the analysis of *in vitro* polarized CD4^{Th17} and CD4^{iTreg} cells (parts created with Biorender.com).

(C) FACS analysis of CD4$^+$ T cells from WT and *Irf4*$^{-/-}$ mice grown in the presence of Th17/Treg-polarizing cytokines.

(D) Liquid chromatography (LC)-MS label-free quantification (LFQ) intensity values for selected cell-type-specific proteins. Data are represented as the mean ± SD. **adj. p (limma) < 0.01; *adj. p (limma) < 0.05; ns, not significant.

(E) Heatmap of proteins with significantly different expression levels in CD4^{Th17} and CD4^{iTreg} cells from WT and *Irf4*$^{-/-}$ mice (adj. p (limma) < 0.01, $|\log_2$(FC *Irf4*$^{-/-}$/WT)| > 1).

(F) PCA of protein abundances.

(G) Numbers of differentially regulated proteins between naive CD4$^+$ T (0 h) cells and CD4^{Th17} and CD4^{iTreg} (72 h) cells and between *Irf4*$^{-/-}$ and WT mice. Numbers next to the arrows indicate the overall numbers of differentially expressed proteins (including up- and downregulated proteins) between the different conditions (see also Figure S3).

(H) Reactome pathway analysis of proteins that were upregulated upon differentiation (day 3 as compared to day 0) in an IRF4-dependent manner and/or in CD4^{Th17} and CD4^{iTreg} cells from WT versus *Irf4*$^{-/-}$ animals.

T cells (0 h) to $CD4^{Th17}$ and $CD4^{iTreg}$ cells (72 h), a total of 2,664 proteins and 2,781 proteins, respectively, changed their expression patterns (Figure 1G and Table S1). This number was also similar for $CD4^{iTreg}$ from *Irf4*$^{-/-}$ mice. However, in *Irf4*$^{-/-}$ $CD4^{Th17}$ cells, the number of proteins with differential expression levels upon differentiation (0 h versus 72 h) was markedly higher (3,164 proteins). This was also reflected in $CD4^{Th17}$ cells at day 3, where around 960 proteins were differentially expressed between *Irf4*$^{-/-}$ $CD4^{Th17}$ cells and $CD4^{Th17}$ cells from WT animals. In $CD4^{iTreg}$ cells, 499 proteins were differentially regulated between WT and *Irf4*$^{-/-}$ $CD4^{iTreg}$ cells, highlighting the more prevalent role of IRF4 for $CD4^{Th17}$ cell development and functionality. Interestingly, *Irf4*$^{-/-}$ cells from both cell types show similar protein expression patterns (Figure 1E). Among the proteins that differ most in their expression level as compared to WT $CD4^{Th17}$ and $CD4^{iTreg}$ cells ($p < 0.01$, $\log_2$(FC *Irf4*$^{-/-}$/WT) > 1 or < −1), we found a strong enrichment of proteins associated with signal receptor (regulator) activity, transcription co-activator binding, and hydrolase activity. Additionally, almost all the proteins are involved in $CD4^{Th17}$ and/or $CD4^{iTreg}$ cell differentiation, displaying differential expression levels at 0 and 72 h in the cells (Figure 1E). These include, e.g., (phospho)proteins associated with signaling receptor activity (cluster 1, Figures 1E and S1) that are involved in protein (kinase) binding, the regulation of cell proliferation, or motility and locomotion or are linked with (ab)normal adaptive (cell-mediated) immunity. This group comprises IRF4 itself; cell-surface receptors CD28, FAS, and CD69; adapter molecules (e.g., TRAF1); the TF NFAT5; MO4L2; and RGCC, as well as kinases such as CDK6 and FADK1 (*Ptk2*). Another protein cluster (cluster 3, Figures 1E and S2) is involved in signaling receptor regulator activity and associated with the positive regulation of $CD4^+$, alpha-beta T cell activation, regulation of metabolic processes, and interspecies interaction between organisms, including proteins involved in the defense against intracellular pathogens as well as (ab)normal T cell physiology and number. Examples are multiple TFs (including FOXP3, FOXP1, IRF1, IRF8, JunD, and TCF-12), cell-surface receptors LRB4A (*Lilrb4a*) and CD166, and IL2RG, which is involved in iTreg cell differentiation, as well as cytokines involved in Treg cell development (e.g., XCL1), Nedd4, and other E3 ubiquitin-protein ligases.

Additionally, we performed Gene Ontology (GO) enrichment analyses exclusively for those proteins that are upregulated under Th17- and Treg-polarizing conditions and displayed different expression levels between *Irf4*$^{-/-}$ and WT cells (Figures 1H and S4 and Table S2). Upon lack of IRF4, proteins associated with protein binding; cellular metabolism, in particular protein and RNA metabolism; and pathways such as glycolysis were affected in both cell types, i.e., $CD4^{Th17}$ and $CD4^{iTreg}$ cells. Metabolic pathways are typically "rewired" upon activation and differentiation of resting lymphocytes, shifting from oxidative phosphorylation to aerobic glycolysis, fulfilling the bioenergetic demands of proliferation and differentiation.[16] IRF4-driven metabolic switch toward glycolysis has been demonstrated before for $CD8^+$ T[17] and Treg cells,[7] which is in line with our data. Distinct metabolic programs have also been associated with the polarization along the Th17 cell and Treg cell axis, correlating oxidative phosphorylation with a Treg cell phenotype.[18] Indeed, proteins involved in oxidative phosphorylation are upregulated in *Irf4*$^{-/-}$ $CD4^{Th17}$ cells and downregulated in *Irf4*$^{-/-}$ $CD4^{iTreg}$ cells (Figure S4). In addition, we observed other marked differences indicating a subtype-specific role of IRF4 in the Th17/iTreg cellular context. Namely, in $CD4^{iTreg}$ cells, we found that mainly pathways regulating processes on the "protein level" were affected, such as protein post-translational modification, protein localization, and (mitochondrial) translation. In contrast, pathways and cellular processes that regulate (downstream) gene expression and transcription were impaired in *Irf4*$^{-/-}$ $CD4^{Th17}$ cells. Additionally, we found that the expression of proteins associated with signal transduction and immune cell functions (e.g., cytokine signaling or Toll-like receptor 2 [TLR2] cascade) were majorly affected by the lack of IRF4 in $CD4^{Th17}$ cells.

Interestingly, a subset of *Irf4*$^{-/-}$ $CD4^+$ T cells cultured under Th17-inducing conditions displayed an increased expression of FOXP3 (34.8%) (Figure 1C). Beside significantly increased FOXP3 levels, proteomic data of *Irf4*$^{-/-}$ $CD4^{Th17}$ cells revealed an elevated expression of other proteins associated with a more "Treg cell-like" phenotype (Figure 1D), such as IRF8,[19] FOXP1,[20] CD166 (*Alcam*),[21] and SMYD,[22] indicating a crucial role of IRF4 in Th17-Treg cell plasticity.

IRF4-mediated gene transcription is regulated by a subset-specific protein complex conserved across the Th17 cell and Treg cell axis

In an effort to discern which proteins act in concert with IRF4 and drive either a Th17 or a Treg phenotype, we determined the cell-type specific IRF4 interactome in $CD4^{Th17}$ and $CD4^{iTreg}$ cells by AP-MS (Figure 2A). To this end, we generated *in vivo*-biotin-tagged IRF4 using the transgenic $ROSA26^{BirA}$ mouse strain,[14] which we crossed with transgenic mice expressing Avi-tagged IRF4 under the control of the endogenous *Irf4* promoter ($IRF4^{Avi\text{-}tag}$ mice, Figures 2B and S5). The offspring ($IRF4^{Bio}$ mice) express biotinylated IRF4 at endogenous levels (Figures 2C and S6). $IRF4^{Bio}$ mice are viable and fertile and show no overt phenotype. No difference could be observed between $CD4^{Th17}$ or $CD4^{iTreg}$ cells derived from $IRF4^{Bio}$ or littermate control mice, indicating that the expression of biotinylated IRF4 is not deleterious to Th17 or Treg cell development (Figures 2D, 2E, S7, S8, and S9). As we were mainly interested in the IRF4 network steering transcriptional regulation, with IRF4 primarily located in the nucleus (exemplarily shown for $CD4^{Th17}$ cells; Figures 2D, S7, and S10), interactome analysis was conducted with the nuclear fraction. To efficiently reduce unspecific background, while at the same time preserving weak interactions, we applied a cell-permeative cross-linker, dithiobis[succinimidyl propionate] (DSP) (Figure S11). Using DSP, PPIs can be preserved *in situ* prior to cell lysis and nuclear extraction (while cells are still alive).[23] Moreover, we could markedly reduce unspecific binding, as we were able to use more stringent wash conditions while concomitantly detecting higher numbers of interaction partners, including previously described IRF4 binding partners such as the TFs Ikaros and Aiolos,[24] at subcellular resolution (Figures 2F and S11–S13 and Table S3).

The optimized protocol was used to define the nuclear IRF4 protein interaction network in $CD4^{Th17}$ and $CD4^{iTreg}$ cells. Combining data from three independent AP experiments, we

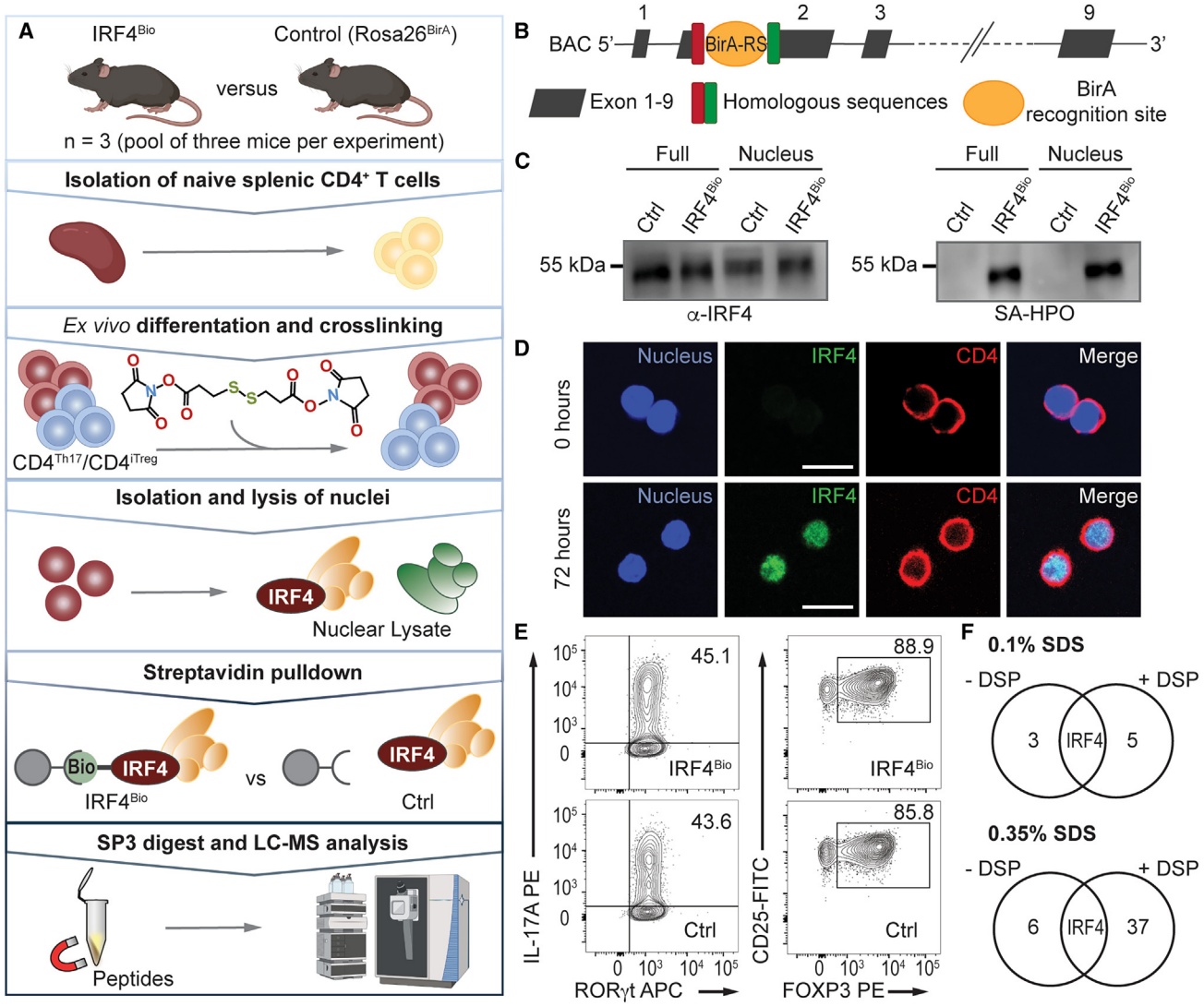

Figure 2. Affinity-purification of endogenous IRF4 complexes

(A) Workflow for the characterization of IRF4 complexes from $CD4^{Th17}$/$CD4^{iTreg}$ cells (parts created with Biorender.com).

(B) BAC transgene for the generation of the $IRF4^{Bio}$ mouse.

(C) Western blot analyses of full cellular lysates and nuclear extracts demonstrate successful *in vivo* biotinylation of IRF4 (left, anti-IRF4 antibody; right, horseradish peroxidase-conjugated streptavidin [SA-HPO]), exemplarily shown for $CD4^{Th17}$ cells.

(D) $CD4^{Th17}$ cells show strong nuclear expression of IRF4 3 days after isolation and *ex vivo* differentiation (white scale bar: 10 μm).

(E) FACS analysis of murine $CD4^{Th17}$ and $CD4^{iTreg}$ cells.

(F) Chemical cross-linking combined with stringent washes improves the quality and specificity of IRF4 pull-down experiments. Venn diagrams display identified IRF4 interaction partners in splenocytes derived from $IRF4^{Bio}$ and control mice.

identified in total of 440 IRF4 interactors across both cell types (Figures 3 and S14 and Table S4). Functional network analysis of these IRF4 interactors drawing upon the STRING database of PPIs indicated a strong network enrichment, where 422 of the 440 candidates (including IRF4) were assigned to a single interconnected network (Figure S14). Several proteins detected in the present dataset have been previously described as interacting with IRF4 in human and/or mouse models, such as Aiolos (encoded by *Ikzf3*), Ikaros (*Ikzf1*), STAT1, STAT3, VPS35, EP300, JunB, and SATB1, as well as members of the Mi-2/nucleosome remodeling and deacetylase (NuRD) complex[24,25] (Table S4).

STRING (search tool for recurring instances of neighbouring genes) network analysis indicated 39 direct associations, functional and/or physical, between IRF4 and the proteins detected by AP-MS, including the Treg and Th17 lineage-defining TFs FOXP3 and RORγt, respectively (Figures 3A and 3B). In total, we identified 53 proteins that were differentially enriched or exclusively detected in either the $CD4^{Th17}$ or the $CD4^{iTreg}$ cell IRF4 interactome (see Figure 3C, 41 proteins enriched in

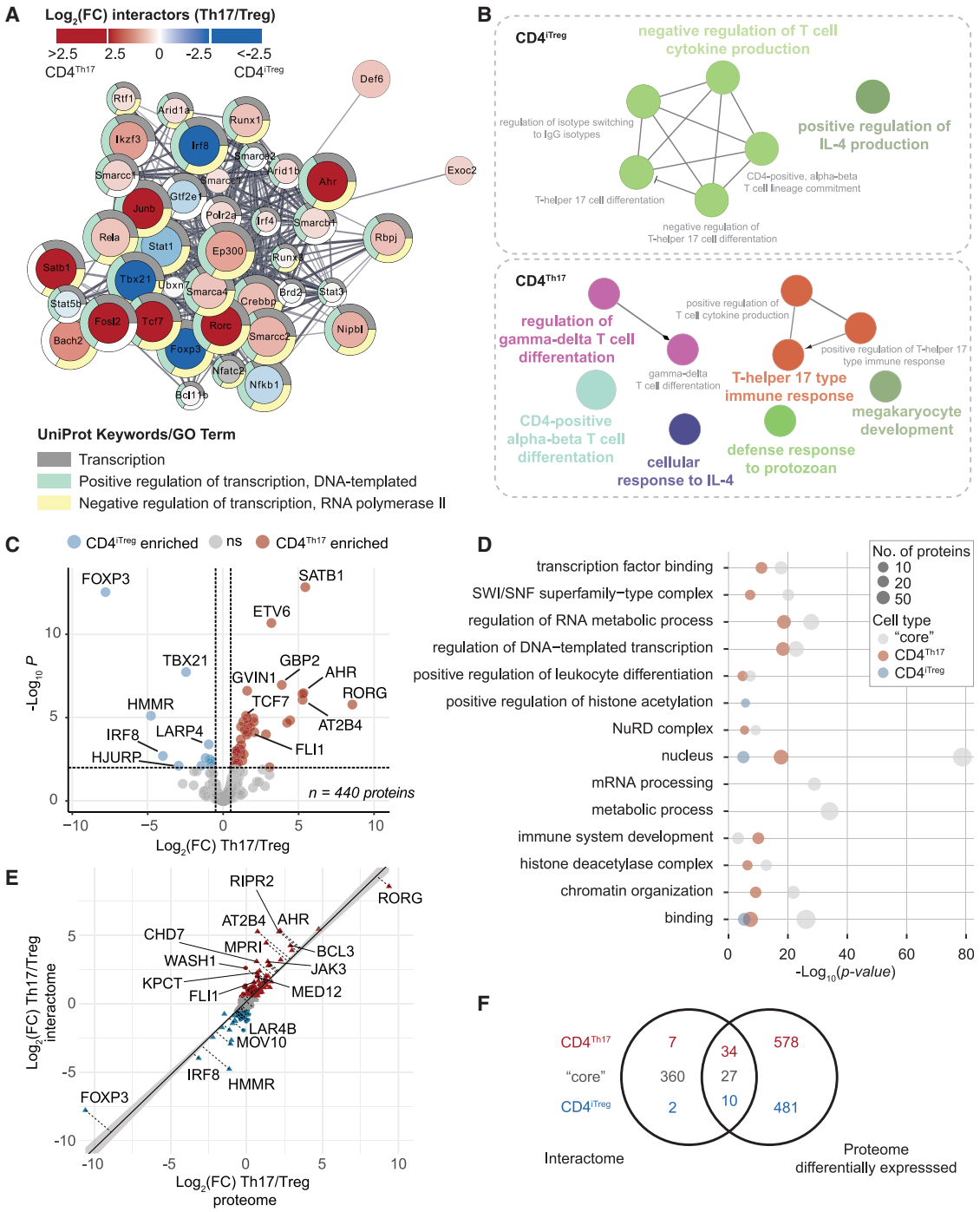

Figure 3. IRF4 interactome analysis reveals different players in IRF4-mediated gene transcription in CD4^{Th17} and CD4^{iTreg} cells

To determine the IRF4 interactome, naive splenic CD4^{+} T cells (pooled from three mice per experiment) were differentiated *ex vivo* under Th17- and iTreg-polarizing conditions for 72 h (three AP-LC-MS experiments/cell type).

(A) STRING-based IRF4 interaction network displaying interactors that have a direct functional and/or physical association with IRF4 (STRING DB default settings; full network is shown in Figure S14). Color scheme indicates enrichment in either CD4^{Th17} (red) or CD4^{iTreg} cells (blue) and node size the level of significance (bigger nodes refer to lower *p* values).

(B) ClueGO analysis of significantly enriched IRF4 in CD4^{Th17} or CD4^{iTreg} cells (adj. *p* (limma) < 0.01, $|\log_2(\text{FC Th17/iTreg})| > 0.5$).

(C) Volcano plot displaying differentially enriched IRF4 interactors in CD4^{Th17} and CD4^{iTreg} cells (adj. *p* (limma) < 0.01, $|\log_2(\text{FC Th17/iTreg})| > 0.5$).

(legend continued on next page)

$CD4^{Th17}$ cells and 12 proteins in $CD4^{iTreg}$ cells). Beside the lineage-defining TFs, these include other characteristic (transcription) factors known to drive cell-type-specific functions (Figure 3B): in $CD4^{iTreg}$ cells, FOXP3, TBX21, and LAT1 (*Slc7a5*) negatively regulate Th17 cell differentiation while promoting IL-4 production required for Treg-mediated immune suppression.[26] Additionally, we found a strong enrichment of IRF8, a silencer of Th17 cell differentiation programs,[27] and of the hyaluronan-mediated motility receptor (HMMR). In the $CD4^{Th17}$ cell IRF4 interactome, we detected ARID5A, MALT1, RORγt, BCL-3, and SATB1, which promote $CD4^{+}$ alpha-beta T cell differentiation and induce Th17 cell-specific immune responses (Figure 3B and Table S5). For example, SATB1 differentially regulates gene expression in Th17 cells, promoting the pathogenic effector program of encephalitogenic Th17 cells.[28] The NF-κB regulator MALT1 determines the encephalitogenic potential of inflammatory Th17 cells in experimental autoimmune encephalomyelitis, a mouse model of multiple sclerosis.[29] However, it has not been associated with IRF4-regulated transcription in the respective study. Other IRF4-interacting proteins enriched in $CD4^{Th17}$ cells, steering lineage-specific gene expression, include CBP/EP300, TCF7, AHR, Fosl2, CHD7, ZN609, BACH2, JunB, and ETV6.[5,30] Whereas JunB has been described as co-localizing with IRF4 at the *Il17* (and *Il21*) promoter[31] and is essential for IL-23-dependent pathogenicity of Th17 cells,[32] other factors, such as TCF7, FLI1, BACH2, and GTF2I, have not been associated with the IRF4 transcriptional regulatory network in Th17 cells. TCF7 (transcription factor 7 or T cell factor 1, TCF1), a major positive regulator of chromatin accessibility required for early T cell development, has been linked with a stem-like Th17 cell state[33] and Th17 longevity.[34] Interestingly, TCF7 expression is reduced and fine-tuned by FOXP3 to drive Treg cell-specific repression of chromatin accessibility and gene expression.[35] Although BACH2 has not been described as a direct interaction partner of IRF4 in Th17 cells, it has been shown that BACH2 directly steers and attenuates T cell receptor (TCR)-induced IRF4-dependent transcription in Treg cells.[36]

Interestingly, we identified a large number of shared IRF4 interactors in both cell types, indicating common regulatory mechanisms (Figure 3C). For proteins identified in the IRF4 "core" interactome in both cell types, i.e., that display no significant enrichment in either $CD4^{iTreg}$ or $CD4^{Th17}$ cells, GO analysis revealed a strong enrichment of nuclear proteins involved in DNA-templated regulation of transcription, many of them displaying TF, DNA, or poly(A) RNA binding capabilities (Figures 3D and S15 and Table S5). Moreover, proteins involved in chromatin organization as well as proteins associated with (m)RNA processing and regulation of (RNA) metabolic processes represent the core IRF4 interactome. The majority of proteins identified in the IRF4 core interactome also displayed no differential expression between the two cell types, i.e., in $CD4^{Th17}$ and $CD4^{iTreg}$ cells, at the full proteome level (Figures 3E and 3F and Table S6). Among the respective proteins, we also identified several members of the ATP-dependent chromatin remodeling complex NuRD, a global modulator of transcription, which acts broadly at many enhancers and promoters to dampen and fine-tune active gene expression.[37] By targeting the NuRD complex, (IRF4-)Ikaros and Aiolos influence its genomic localization and functional activity.[24,38] Additionally, we detected the chromatin-remodeling SWI/SNF (switch/sucrose nonfermenting) complex, which plays, as transcriptional activator, an antagonistic role against NuRD on common regulatory elements.[37] Both complexes are required during cellular commitment "decisions" regulating both B and T cell differentiation (forming together with Ikaros the so-called PYR complex). Data derived from T cells suggest that NuRD/Mi-2 can determine the transcriptional activity of TFs in a stage-specific manner and that concomitant interactions between functionally opposing chromatin-regulating machineries are an important mechanism of gene regulation during lineage determination.[39] Other core interactors are protein kinases (e.g., CDK7, CDK2, CDK1, and CDK9) involved in cell-cycle control, RNA transcription, and regulation of gene expression. CDK9, for example, steers cytokine-inducible transcription networks (such as IL-6-inducible STAT3 signaling), whereas CDK2, by phosphorylating FOXP3, negatively regulates its transcriptional activity and protein stability.[40]

ChIP-seq analysis reveals a strong enrichment of motifs from IRF4 binding partners

To identify target genes regulated by the IRF4 complexes in $CD4^{Th17}$ and $CD4^{iTreg}$ cells, we performed Bio-ChIP-seq (Figure 4 and Table S7). ChIP-seq analysis of IRF4 in $CD4^{Th17}$ cells revealed 21,884 IRF4 binding regions annotated to 10,918 unique genes. Most peaks in the $CD4^{Th17}$ cells (41.9%) were found in the promoter region (up to 3 kb downstream of the transcription start site [TSS]), followed by intronic binding (26.2%) and distal intergenic binding (26.0%) (Figure 4B). In $CD4^{iTreg}$ cells, a total of 10,189 binding regions were detected, corresponding to 5,789 genes. Binding of IRF4 was most prevalent in introns (32.9%) followed by promoter binding (31.9%) and distal intergenic binding (31.0%) (Figure 4B). A total of 5,314 genes showed IRF4 binding in $CD4^{Th17}$ and $CD4^{iTreg}$ cells, while 5,604 genes were exclusively bound in $CD4^{Th17}$ cells and 475 genes in $CD4^{iTreg}$ cells. The high number of IRF4-regulated genes in $CD4^{Th17}$ cells along with the large number of associated promoter regions is in line with previous findings and further underlines the more prevalent role of IRF4 in $CD4^{Th17}$ as compared to $CD4^{iTreg}$ cells. Moreover, in line with previous studies,[5,6] we could confirm IRF4 binding in the promoter regions of the *Il17a* and *Rorc* genes. Of note, distinct IRF4 binding sites were detected within in the distal intergenic, intron, and promoter regions of *Il17a* and *Rorc* exclusively in $CD4^{Th17}$ cells (Figure 4A). In both cell types, we could not detect any binding within the *Foxp3* locus.

Approximately 72% of the $CD4^{Th17}$ peaks mapped to predicted enhancer structures (10,990 unique enhancers) of the $CD4^{+}$ cell data in the Enhancer Atlas 2.0,[41] while 1,477 peaks

(D) GO and reactome pathway analysis of IRF4 interactors. Gray, "core" IRF4 interactome; red, $CD4^{Th17}$, $\log_2$(FC Th17/iTreg) > 0.5; blue, $CD4^{iTreg}$ $\log_2$(FC Th17/iTreg) < −0.5).
(E) Comparison of log-transformed protein fold changes at the interactome and at the proteome level between $CD4^{Th17}$ and $CD4^{iTreg}$ cells.
(F) Overlap of the IRF4 interactome with differentially expressed proteins in $CD4^{Th17}$ versus $CD4^{iTreg}$ cells (full cellular proteome).

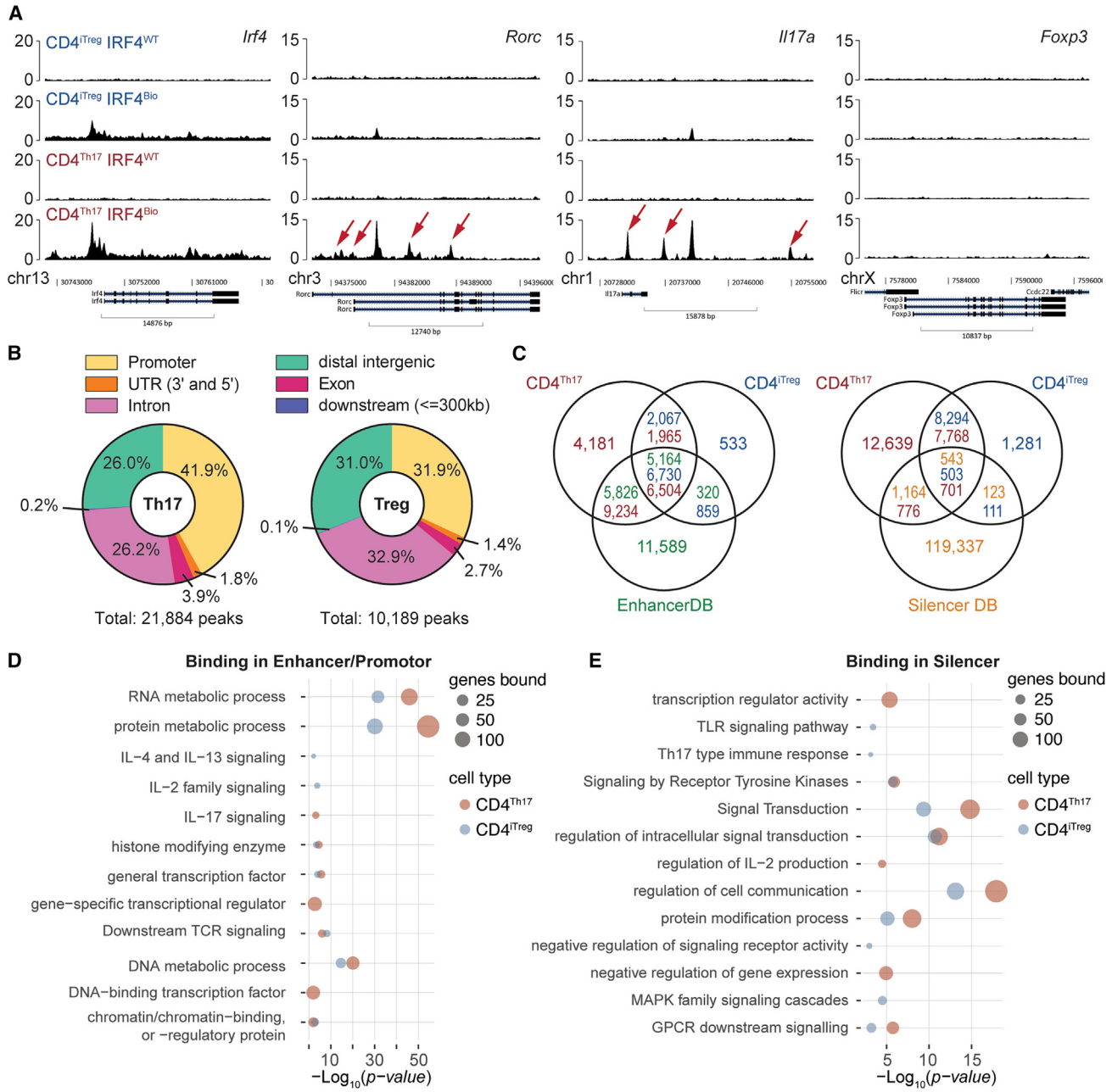

Figure 4. IRF4 ChIP-seq analysis reveals twice the number of regulated genes in CD4^{Th17} compared to CD4^{iTreg} cells

IRF4 Bio-ChIP-seq analysis was performed in CD4^{Th17} and CD4^{iTreg} cells from IRF4^{Bio} mice. Cells derived from ROSA26^{BirA} (IRF4^{WT}) served as control.

(A) ChIP-seq binding tracks for selected loci in CD4^{Th17} and CD4^{iTreg} cells at 72 h.

(B) Distribution of identified binding sites in CD4^{Th17} and CD4^{iTreg} cells.

(C) Overlap of identified binding sites with EnhancerDB[41] and SilencerDB[42] knowledge bases.

(D and E) GO and Reactome pathway analysis of genes bound by IRF4 in (D) enhancer/promoter and (E) silencer regions.

(6.7%) were associated with gene expression silencing (corresponding to 1,707 silencer regions; SilencerDB[42]) (Figure 4C). In CD4^{iTreg} cells, 7,589 peaks (74.5%) showed an overlap with the enhancer database (mapping to 5,484 enhancer structures); among these, 88.7% were shared with CD4^{Th17} cells. Of the 614 peaks (6.0%) mapping to unique silencer structures in CD4^{iTreg} cells, 543 (88.4%) were also detected in CD4^{Th17} cells. Conducting functional enrichment analysis, we found that expression of genes associated with RNA, DNA, and protein metabolic processes is promoted by IRF4 in both CD4^{Th17} and CD4^{iTreg} cells (Figure 4D and Table S8). This ties in nicely with the proteomic data, where we observed a deregulation of RNA, DNA, and

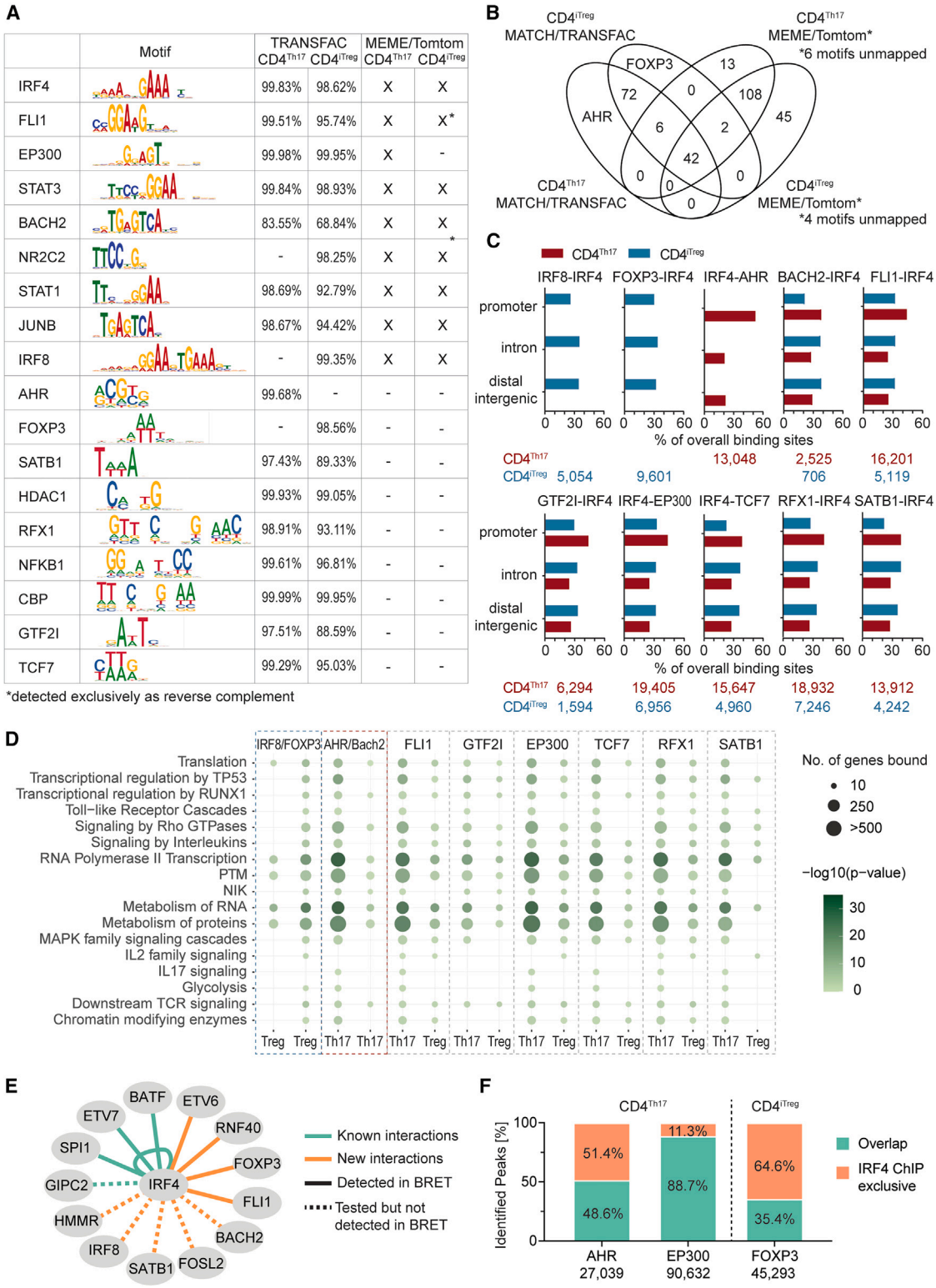

Figure 5. Motif analysis reveals binding sites of IRF4 interaction partners in genes required for metabolic and effector functions of CD4^{Th17} and CD4^{iTreg} cells

(A) Binding motifs of IRF4 interactors were identified and enriched in the IRF4 ChIP-seq data.

(B) Overlap of motifs identified by MATCH/TRANSFAC and MEME/Tomtom in CD4^{Th17} and CD4^{iTreg} cells.

(legend continued on next page)

protein metabolic pathways upon lack of IRF4. In addition, genes promoting the expression of general TFs, histone-modifying enzymes, and chromatin/chromatin binding or regulatory proteins were found to be positively regulated by IRF4 in both T cell types. Elevated gene expression for gene-specific transcriptional regulator or DNA binding TFs was seen only in $CD4^{Th17}$ cells. This is also in line with the proteomic dataset, where we mainly observed an impaired expression of proteins associated with transcription in $CD4^{Th17}$ but not $CD4^{iTreg}$ cells (Figure 1). The expression of genes associated with downstream signaling of the TCR is enhanced by IRF4 in both cell types. However, genes related to IL-17 signaling are promoted only in $CD4^{Th17}$ cells by IRF4, while in $CD4^{iTreg}$ cells, IL-2 (family), IL-4, and IL-13 signaling is increased (Figure 4D). Genes that are silenced by IRF4 in both cell types were mainly associated with signal transduction and the regulation of cell communication. Interestingly, in $CD4^{iTreg}$ cells, IRF4 complexes downregulate Th17-type immune responses as well as TLR and mitogen-activated protein kinase (MAPK) signaling, while in $CD4^{Th17}$ cells, genes related with the regulation of IL-2 production, transcription regulator activity, and the negative regulation of gene expression were silenced (Figure 4E and Table S8). Despite the large number of commonly targeted genes across $CD4^{Th17}$ and $CD4^{iTreg}$ cells, these data further demonstrate that IRF4 additionally acts in a context-dependent, cell-type-specific manner.

To identify TF binding sites within the immunoprecipitated DNA fragments, we conducted a motif analysis using the MATCH algorithm[43] and the murine Transcription Factor (TRANSFAC) database[44] (Figure 5 and Table S7). This revealed binding motifs from 133 unique proteins with the majority, i.e., 129 associated proteins, reported for both cell types (Figures 5A and 5B). Interestingly, the AHR binding motif was exclusively identified in $CD4^{Th17}$ cells, while the FOXP3, IRF8, and NR2C2 motifs were detected only in $CD4^{iTreg}$ cells. The best matching count matrix for IRF4 was described in 21,846 peaks (99.83%) of the $CD4^{Th17}$ ChIP and in 10,048 peaks (98.62%) of $CD4^{iTreg}$ cells, confirming efficient isolation of IRF4 DNA binding regions. Additionally, we applied MEME-ChIP,[45,46] revealing 42 enriched motifs in the DNA fragments of $CD4^{Th17}$ cells and 21 enriched motifs in $CD4^{iTreg}$ cells. To identify TFs associated with the enriched motifs, we used the Tomtom algorithm[47] for motif mapping against the murine TRANSFAC database, revealing 171 matching proteins (for 33 motifs) in $CD4^{Th17}$ cells and 206 unique proteins (for 17 motifs) in $CD4^{iTreg}$ cells (Figures 5A and 5B). Eight motifs in the $CD4^{Th17}$ ChIP and four motifs from the $CD4^{iTreg}$ ChIP were identified as enriched but could not be mapped to any TF from the TRANSFAC database (Figure S17). Enriched motifs mapped to 152 proteins that were reported for both cell types. Of these, 42 TFs were also identified by the MATCH/TRANSFAC algorithm in both $CD4^{iTreg}$ and $CD4^{Th17}$ cells, including IRF4, FLI1, STAT3, BACH2, STAT1, and JunB. All those proteins were also detected in the IRF4 interactome in both cell types, indicating that they act and transcribe genes in concert with IRF4 in $CD4^{iTreg}$ and $CD4^{Th17}$ cells. Although the motif of the IRF4 interactor EP300 was identified by MATCH/TRANSFAC in both cell types, enrichment was reported only in $CD4^{Th17}$ cells. Motifs of IRF8 and NR2C2 were identified as enriched in both cell types but were found only in $CD4^{iTreg}$ cells by the MATCH/TRANSFAC algorithm. Additional motifs identified by MATCH/TRANSFAC mapped to SATB1, HDAC1, RFX1, NFKB1, CBP, GTF2I, and TCF7, all identified also in the IRF4 interactome.

IRF4, which on its own displays only weak DNA binding affinity, typically associates with other TFs, e.g., PU.1 and Spi-B in B cells or AP1 in $CD4^+$ T cells, resulting in the recruitment of the (heterodimeric) complex to composite motifs (ETS-IRF or AP1-IRF4 composite elements, referred to as EICE/AICE motifs) in the genome.[6,48,49] Conducting a combined motif analysis to identify motifs in close proximity to each other (up to 5 bp distance; Figure 5C and Tables S7 and S9), we found that nearly all previously detected motifs of IRF4 interactors were located in the immediate vicinity of the IRF4 motif. Additionally, the motifs of IRF4 interactors were also detected in close proximity to one another (Table S7). In line with the single motif analysis, FOXP3-IRF4 and IRF8-IRF4 composite motifs were exclusively identified in the $CD4^{iTreg}$ ChIP-seq dataset, while IRF4-AHR composite elements were exclusively reported for $CD4^{Th17}$ cells. The FOXP3-IRF4 motif is the most prominent composite motif in $CD4^{iTreg}$ cells (around 9,601 associated peaks), followed by RFX1-IRF4 and IRF4-EP300 motifs. In $CD4^{Th17}$ cells, we found multiple composite motifs that were associated with a high number of target genes, including IRF4-AHR, FLI-IRF4, IRF4-EP300, IRF4-TCF7, RFX1-IRF4, and SATB1-IRF4 (13,000 to >19,000 peaks). In addition, most of these coincident binding peaks are located in promotor regions, suggesting a driving role for the respective IRF4 interactors in maintaining Th17 functionality. This could be further confirmed by GO analysis. Target genes containing composite motifs and associated with IL-17 signaling and glycolysis are co-regulated by IRF4 and AHR, FLI1, EP300, TCF7, RFX1, and SATB1 in $CD4^{Th17}$ cells (Figure 5D and Table S10). Additionally, we found that genes associated with TLR signaling are mainly targeted in $CD4^{Th17}$ but not in $CD4^{iTreg}$ cells. In general, GO analysis revealed similar gene regulatory patterns for IRF4 complexes between $CD4^{iTreg}$ and $CD4^{Th17}$ cells. However, it should be noted that the proportion of peaks positioned in intronic regions was much higher in $CD4^{iTreg}$ cells as compared to $CD4^{Th17}$ cells, where IRF4 complexes and heterodimers favor promoter binding.

To further validate our findings, we conducted a bioluminescence resonance energy transfer (BRET)-based PPI assay,[50] probing the binding of IRF4 to selected potential partner proteins (Figures 5E and S16 and Table S11). So far, there are only a few

(C) Distribution of IRF4 composite motifs across the peaks identified by IRF4 ChIP-seq (IRF4 and indicated interactor within a proximity of 5 bp). Total number of peaks where combined motifs were detected is indicated below the bar plots.
(D) Reactome analysis of genes regulated by IRF4 and its interactors in $CD4^{Th17}$ and $CD4^{iTreg}$ cells.
(E) Binary IRF4 interactions identified by BRET.
(F) Proportion of IRF4 peaks containing composite motifs covered by public ChIP-seq datasets (green, overlap with public dataset; orange, exclusively detected in the IRF4 Bio-ChIP-seq dataset; see also Figure S17).

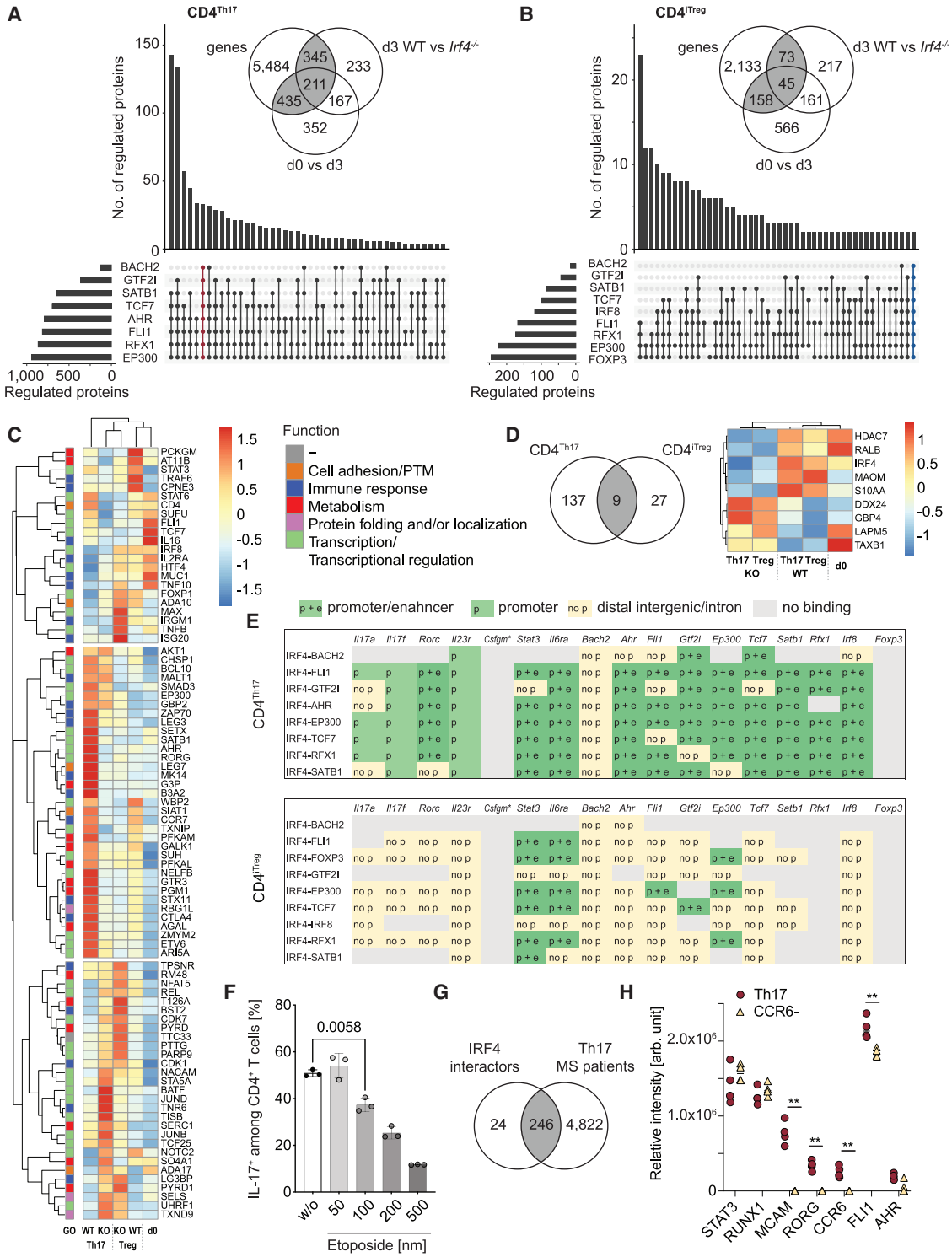

Figure 6. Genes regulated in CD4^{Th17} and CD4^{iTreg} cells display altered proteomic patterns in *Irf4*$^{-/-}$ animals

(A and B) Number of genes regulated by IRF4 and distinct interactors in (A) CD4^{Th17} and (B) CD4^{iTreg} cells. Insets show an overlap of regulated genes (filtered for IRF4 binding in "promoter + enhancer" or "promoter + silencer" regions), IRF4-dependent differentially expressed proteins at day 0 and day 3, and differentially expressed proteins in CD4^{Th17} and CD4^{iTreg} cells from *Irf4*$^{-/-}$ and WT mice (see also Figure S19).

(C) Protein expression patterns of selected candidates regulated by the IRF4 complex that display differential protein levels upon IRF4 knockout.

(D) Genes (proteins) regulated by IRF4 that show the same patterns in CD4^{Th17} and CD4^{iTreg} cells.

(legend continued on next page)

proteins for which a direct, binary interaction with IRF4 was experimentally shown. These include GIPC2, ETV7, PU.1 (SPI1), and BATF,[51] which we selected as positive controls. Of the four positive controls, binding to IRF4 was observed for PU.1, ETV7, and BATF (detected also in the $CD4^{Th17}$ interactome of the present study; Figure S14). Among the tested candidates (see Figures 5E and S16), we could confirm, using two different approaches, binary interactions between IRF4 and the partner proteins ETV6, RNF40 (BRE1B), FOXP3, and FLI1. Additionally, we demonstrated IRF4 homodimerization. Of note, human homologs of IRF4 and its interactors were used for BRET measurements, demonstrating that our findings from the murine model can be transferred (to a certain extent) also to the human model.

Additionally, we screened public repositories for further validation and identified different datasets where ChIP-seq analyses of AHR, EP300, and FOXP3 were performed in murine Th17 (AHR and EP300) and iTreg cells (FOXP3) (Figures 5F and S17). We investigated which of the IRF4 double-motif-containing peaks from our Bio-ChIP-seq dataset were also detected in the public datasets. Overall, we found a high overlap, particularly in the case of EP300. Here, public datasets cover over 88% of identified peaks from our dataset containing IRF4-EP300 double motifs ($CD4^{Th17}$). In the case of IRF4-AHR ($CD4^{Th17}$), up to 48.6% of peaks overlapped, and up to 35.4% in the case of IRF4-FOXP3 ($CD4^{iTreg}$), indicating along with the interactome data of the present study that, indeed, a co-binding to these sites takes place.

FLI1 is required for $CD4^{Th17}$ functionality

To investigate which proteins are directly affected by the IRF4-driven gene regulation, we integrated the information derived from the interactome, Bio-ChIP-seq, and *Irf4*$^{-/-}$ proteome analyses (Figure 6). To this end, we analyzed which proteins correspond to genes that are targeted by IRF4 heterodimers (i.e., multimers) and are affected by the lack of IRF4 (Figures 6A and S18 and Table S1). In total, we identified 1,017 proteins in $CD4^{Th17}$ cells that showed deregulated expression patterns upon differentiation (day 0 versus day 3) and/or in fully differentiated $CD4^{Th17}$ cells (day 3) between WT and *Irf4*$^{-/-}$ animals and were directly regulated on the gene level by IRF4 and distinct interactors (binding in either the "promoter + enhancer" or the "promoter + silencer" region). In $CD4^{iTreg}$ cells, this was the case for 280 proteins (Figures 6A and S18). Among these proteins, we detected a large number of TFs, including IRF4 interactors, as well as proteins associated with cellular metabolism and the immune response (Figure 6C). Nine proteins targeted by IRF4 displayed similar protein expression patterns in both cell types upon differentiation and lack of IRF4, indicating common regulatory mechanisms (Figure 6D). These include the histone deacetylase 7, which enhances the transcriptional repressor activity of FOXP3 (by similarity, UniProt); the GTPases RALB and GBP4; the mitochondrial NAD-dependent malic enzyme 2 (ME2), crucial for mitochondrial pyruvate and energy metabolism[52]; and TAXB1 and LAPM5, involved in the (negative) regulation of T cell activation and NF-κB signaling (Figure 6D).

In $CD4^{Th17}$ cells, regulated proteins are mainly associated with transcriptional regulation and Th17 cell differentiation as well as glucose metabolism (Figures 6C, 6E, S19, and S20). Interestingly, TFs and transcriptional regulators that are part of the IRF4 interactome, such as AHR, EP300, FLI1, ETV6, RORγt, TCF7, SATB1, MALT1, ZMYM2, ARI5A, and SUFU, are transcriptionally regulated by the IRF4 complex itself in $CD4^{Th17}$ cells and display low protein expression levels upon the lack of IRF4, indicating a positive feedback regulation for the respective gene products (Figures 6C and 6E). In $CD4^{iTreg}$ cells, gene expression of proteins involved in protein localization, lipid and rRNA binding/translocation, as well as transcriptional regulation, is directly steered by the IRF4 complex. Examples of transcriptionally regulated proteins that display aberrant expression upon lack of IRF4 in $CD4^{iTreg}$ cells are TRAF6, required for post-translational FOXP3 regulation[53]; Copine-3; and the phospholipid-transporting ATPase IF, involved in cell migration and the maintenance of membrane lipid asymmetry in the endosomal compartment.

To further validate our findings, we assessed the effect of FLI1 inhibition on Th17 cell differentiation. The FLI1-IRF4 composite motif was enriched in our Bio-ChIP-seq dataset, particularly in promoter/enhancer regions of genes relevant for a Th17 phenotype (Figures 6E and S21). Moreover, binary interactions between IRF4 and the Ets family member FLI1, enriched in the Th17 interactome, were confirmed by BRET. IRF4-Ets1 complexes are known to assemble in B cells, suggesting a similar molecular mechanism in the case of T(h17) cells. Hence, we tested the effect of FLI1 inhibition on Th17 cell differentiation, observing markedly reduced numbers of Th17 cells among the population of $CD4^+$ T cells upon addition of the FLI1 inhibitor etoposide[54] (Figures 6F and S21). As AHR-IRF4 composite motifs were exclusively enriched in CD4Th17 cells, we also evaluated the effect of AHR inhibition on Th17 cell differentiation using BAY2416964[55] and resveratrol[56] (Figure S22). While we observed a marked cytotoxic effect when treating cells with resveratrol, cells showed still good viability upon BAY2416964 addition, and the numbers of FOXP3-expressing cells increased. However, the percentage of Th17 cells among $CD4^+$ cells was not markedly affected.

Additionally, we evaluated if proteomic signatures of murine $CD4^{Th17}$ cells are similar in human Th17 cells by isolating Th17 cells from the peripheral blood of multiple sclerosis patients (n = 4) (Figures 6G, 6H, and S23 and Table S12). $CD3^+CD4^+CD45RO^+CCR6^+MCAM^+$ Th17 cells and a $CCR6^-$

(E) IRF4 DNA binding patterns in $CD4^{Th17}$ and $CD4^{iTreg}$ cells for genes targeted by the IRF4 complex. Composite motifs indicate co-regulation of the respective gene by IRF4 and its binding partner(s). Binding in promoter-enhancer region (p + e), promoter region (p), and distal intergenic or intron regions (no p) is shown; gray indicates no binding detected or no peaks identified in target gene containing the respective IRF4 composite motif.
(F) FLI1 inhibition by etoposide impairs Th17 differentiation. Data are represented as the mean ± SD. Number above bars indicates the p value of the comparison between control (w/o) and etoposide-treated cells (100 nM, two-tailed Welch's t test).
(G) Overlap between identified murine $CD4^{Th17}$ IRF4 interactors and the proteome of Th17 cells isolated from multiple sclerosis patients (n = 4).
(H) LC-MS-based LFQ intensity values for selected cell-type-specific proteins in patient-derived Th17 cells and matching $CCR6^-$ cell populations (n = 4). $^{**}p < 0.01$; Benjamini-Hochberg corrected p-value (Student's t test).

control population were directly sorted into an SDS lysis buffer and subsequently prepared for MS-based proteome analysis. In total, 246 of the 270 IRF4 interactors in Th17 cells were also expressed in human Th17 cells (248 including 2 candidates identified in only two of four patients). Of note, comparing the human Th17 cell population with CCR6$^-$ cells, we detected an increased expression of FLI1, required for Th17 differentiation in the murine model.

DISCUSSION

IRF4 is crucial for the fate determination of pro-inflammatory Th17 cells and the functionally opposing group of iTreg cells.[2,3,8,9] Although numerous studies have explored IRF4-mediated transcriptional programs in (differentiating) Th17 and Treg cells, no study so far has focused on a side-by-side comparison of both cell types. Here, we integrate discovery-based proteome analysis of CD4$^+$ T cells polarized under Th17- and iTreg-skewing conditions from WT and *Irf4*$^{-/-}$ animals with IRF4 Bio-ChIP-seq and interactome analyses, providing an unbiased view on the molecular mechanisms of IRF4-driven gene expression and interactions at a late time point of differentiation. Consistent with previous research,[2] we show that IRF4 has a stronger impact on CD4^{Th17} compared to CD4^{iTreg} cells. While CD25$^+$ FOXP3$^+$-expressing iTreg cells could develop from *Irf4*$^{-/-}$ naive CD4$^+$ T cells, Th17 cell development was markedly impaired in the absence of IRF4. No IL-17-secreting cells were detected by fluorescence-activated cell sorting (FACS), and proteomic characterization revealed more dysregulated proteins in *Irf4*$^{-/-}$ CD4^{Th17} compared to *Irf4*$^{-/-}$ CD4^{iTreg} cells. This was further affirmed by Bio-ChIP-seq analysis identifying twice as many IRF4 binding sites, especially in the promoter regions, in CD4^{Th17} cells.

Additionally, we performed IRF4 interactome analyses in both cell types, which revealed a large number of common IRF4 interactors, including members of the NuRD and SWI/SNF complexes as well as proteins associated with the regulation of DNA-templated transcription and mRNA processing, while other interactors were subtype specific. Literature cross-referencing verified several IRF4 interactors (Table S4), but also uncovered additional associations with proteins like FLI1, BACH2, AHR, GTF2I, RFX1, and MALT1, among many others, which were previously undescribed. Moreover, the majority of known IRF4 interactions have been associated with other (immune) cell types, e.g., macrophages,[57] plasma cells,[24] or other T cell subsets,[12] but not with Th17/Treg cells. To our knowledge, in Treg cells, only a FOXP3-IRF4 interaction was demonstrated, which regulates the expression of genes essential for the anti-inflammatory character of this cell type, e.g., *Icos*, *Il10*, or *Grmb*.[8,9] An interaction of IRF4 with (BATF-)JunB[6,48] or STAT3[2,9] in Th17 cells was described by co-localization and overlapping DNA binding regions of those TFs at Th17-critical genes, such as *Rorc*, *Il17a*, *Il17f*, and *Il21*[5,58]; however, no physical interaction could be verified by reproducible immunoprecipitations.[6,58]

IRF4 typically associates with cell-type-specific partners to bind distinct composite sequence elements,[48,49] such as the AICE and ISRE composite elements in T and B cells as well as the EICE and ZICE motifs in B cells. Numerous motifs targeted by IRF4 interactors were enriched in our Bio-ChIP-seq data. Motif analysis revealed several IRF4 composite elements for TFs, such as BACH2, FLI1, GTF2I, EP300, TCF7, RFX1, and SATB1, that have not been described before. Some motifs were unique to one cell type, such as the "IRF8-IRF4" and "FOXP3-IRF4" elements in the case of CD4^{iTreg} and the "IRF4-AHR" motif in the case of CD4^{Th17} cells. Comparing to public ChIP-seq datasets of AHR, EP300, and FOXP3, we found a high overlap of peaks containing the respective IRF4 composite DNA elements, particularly for EP300, suggesting that, indeed, a co-binding to these sites takes place. Probing binding of IRF4 to selected partners by BRET, we could confirm binary interactions between IRF4 and the partner proteins ETV6, RNF40 (BRE1B), FOXP3, and FLI1 and demonstrate IRF4 homodimerization.

Linking IRF4-regulated genes (IRF4 binding in either promoter + enhancer or promoter + silencer regions) with the *Irf4*$^{-/-}$ proteome dataset, we could identify a set of genes targeted by IRF4 and distinct interactors for which aberrant expression was also observed at the proteome level (i.e., for the respective gene product). These include proteins associated with immune response and metabolism as well as a large number of transcriptional regulators. Interestingly, among the transcriptional regulators, we identified several IRF4 binding partners, e.g., AHR, FLI1, EP300, TCF7, GTF2I, RFX1, SATB1, etc., that bind in concert with IRF4 to their own promoter region, suggesting a positive feedback regulation for the respective molecules in CD4^{Th17} cells. The IRF4-FLI1 composite element, for example, was also identified in the promoter/enhancer regions of genes regulating Th17 functions (*Il17a*, *Il17f*, *Rorc*, *Stat3*, *Il6ra*, and glycolysis-associated genes). Binary interactions between IRF4 and the Ets family member FLI1 by BRET suggest similar molecular mechanisms in the case of T as for B cells, where IRF4-Ets1 complexes are known to assemble, promoting transcriptional processes.[48] Indeed, Th17 differentiation was impaired during *ex vivo* polarization of CD4$^+$ T cells under 17-skewing conditions in the presence of the FLI1 inhibitor etoposide. FLI1 has been previously associated with the development of pro-inflammatory diseases, such as graft-versus-host disease (GVHD), colitis, and lupus,[59–61] and a low dose of etoposide attenuated GVHD severity.[54] Moreover, *Fli1*$^{-/-}$ studies demonstrated a downregulation of genes associated with pro-inflammatory states, while genes with anti-inflammatory properties were upregulated.[59–61] Additionally, metabolic pathways were affected by FLI1 knockout in T cells, which displayed decreased glycolytic but increased oxidative phosphorylation activity.[54] Here, we could demonstrate a direct association between IRF4 and FLI1, which is required for the regulation of Th17-associated transcriptional programs. Notably, analyzing the proteome of CCR6$^+$MCAM$^+$ Th17 cells derived from multiple sclerosis patients, we found an increased expression of FLI1 as compared to the CCR6$^-$ control population.

Although we could demonstrate a binary interaction between IRF4 and FOXP3 and identify IRF4-FOXP3 composite elements in CD4^{iTreg} cells, no binding was observed within the *Foxp3* locus, in neither CD4^{iTreg} nor CD4^{Th17} cells. Our finding that IRF4 does not directly bind to the *Foxp3* locus but interacts, e.g., with SATB1 suggests that IRF4-mediated inhibition of FOXP3 expression is a rather indirect and SATB1-dependent process.

Of note, repression of SATB1 was already demonstrated to be important for Treg cell effector function,[62] further supporting this hypothesis.

In conclusion, we present an integrated analysis of IRF4-mediated gene regulation in $CD4^{Th17}$ and $CD4^{iTreg}$ cells, utilizing Bio-ChIP-seq, interactome, and proteome data. The findings highlight IRF4's predominant role in $CD4^{Th17}$ cells and outline the cell-type-specific gene regulatory networks essential for both Th17 and (i)Treg functionality. Moreover, the present interactome dataset defines lineage-specific, endogenous IRF4 interaction partners within the Th17/Treg context as well as composite DNA motifs targeted by IRF4 complexes, providing a valuable resource for studying IRF4-mediated gene regulatory programs in pro- and anti-inflammatory immune responses.

Limitations of the study

While the present approach allows one to determine IRF4 interactors at endogenous levels, a large number of cells was required for the interactome analysis. Due to this "bulk" approach using $CD4^{Th17}$ and $CD4^{iTreg}$ cells after *ex vivo* polarization, the present method does not resolve interactions that happen sporadically or in a fraction of cells. Although binary interactions were confirmed for a few selected proteins by an independent approach using human homologs, the current study does not resolve detailed binding mechanisms between IRF4 and distinct interaction partners, e.g., on a structural level.

While we could demonstrate FLI1-mediated effects in $CD4^{Th17}$ cell differentiation upon FL1 inhibition, additional genetic approaches would complement the findings presented in this article. This particularly holds true also for the study of the biological relevance of the IRF4-AHR interaction and the interaction of IRF4 with other candidates identified in the present study. Here, transgenic models are required to shed further light on IRF4-mediated transcriptional regulation.

RESOURCE AVAILABILITY

Lead contact

Requests for further information and resources and reagents should be directed to and will be fulfilled by the lead contact, Ute Distler (ute.distler@uni-mainz.de).

Materials availability

Any materials generated in this study can be made available by Ute Distler, the lead contact, upon request.

Data and code availability

- The MS proteomics data have been deposited to the ProteomeXchange Consortium (http://proteomecentral.proteomexchange.org) via the jPOST partner repository[63] with the dataset identifiers PRIDE: PXD044298/jPOST: JPST002260 (murine datasets) and PRIDE: PXD060137/jPOST: JPST003563 (human data). The ChIP-seq data can be accessed on Gene Expression Omnibus (GEO) via the accession no. GEO: GSE240979.
- All source code and data files are available from the authors upon request. The R-scripts used for statistical and ChIP-seq analysis are made available at https://github.com/Muedi/IRF4-in-Treg-and-Th17 and https://doi.org/10.5281/zenodo.14643315.
- Any additional information required to reanalyze the data reported in this work paper is available from the lead contact upon request.

ACKNOWLEDGMENTS

We thank Ruben Spohrer, Stefanie Hesse-Kerolli, and Christina Jung, for excellent technical assistance, as well as Laura Jager and Mariane Gonçalves Kulik for assistance with the BRET experiments and support with data evaluation. This work was supported by the German Research Foundation (DFG; project nos. 318346496 and SFB1292/2 TP01 to T.B., TP11 to U.D. and N.L., and TP-Q1 to S.T. as well as DI 2471/1-1 to U.D. and BO 3306/2-1 to T.B. and project no. 449991970 to K.L.), the DFG priority program SPP 2225 (project no. 446605368 to U.D.), SFB TRR355 (TPA9 and TPA10 to T.B.), and the Research Center for Immunotherapy (FZI) of the Johannes Gutenberg-University Mainz.

AUTHOR CONTRIBUTIONS

T.B. established the transgenic mouse model. A.G., S.D., A.N., K. Romaniuk, and G.B. performed the animal experiments and wet lab work. K.L., M.W., and M.E. conducted and evaluated the BRET experiments. A.G., U.D., and G.H. conducted the microscopic experiments. A.G., B.W., K.P., K.R., and G.B. performed the flow cytometric analysis and U.D. the mass spectrometric analyses. A.G. and M.K. performed the Bio-ChIP-seq analysis. A.G., M.S., M.C., M.K., D.G.-Z., T.Z., and U.D. analyzed the mass spectrometric and Bio-ChIP-seq data. M.S. and M.C. wrote the R-scripts and codes for downstream data analysis and visualization. N.L., S.B., K.L., M.W., K. Rajalingam and S.T. aided the conceptualization of experiments and contributed to writing. U.D. and T.B. designed the project. A.G., M.S., M.C., and U.D. prepared the initial draft of the manuscript. All authors reviewed the final manuscript version.

DECLARATION OF INTERESTS

The authors declare no competing interests.

STAR★METHODS

Detailed methods are provided in the online version of this paper and include the following:

- KEY RESOURCES TABLE
- EXPERIMENTAL MODEL AND STUDY PARTICIPANT DETAILS
  - Animals
  - Isolation of murine splenocytes, naïve $CD4^{+}$ T cells and $CD4^{Th17}$/$CD4^{iTreg}$ differentiation
  - Isolation of human Th17 cells
  - Cell lines
- METHOD DETAILS
  - Antibodies
  - Flow cytometry
  - Flow cytometric collection and handling of human Th17 cells
  - Chemical cross-linking and isolation of nuclei
  - Isolation of IRF4 complexes
  - Proteolytic digestion
  - Western blot analysis
  - Liquid chromatography-mass spectrometry (LC-MS) analysis
  - Chromatin immunoprecipitation coupled with sequencing (ChIP-seq)
  - Immunostaining for confocal fluorescence microscopy
  - Confocal microscopy
  - Plasmid construction
  - BRET assay
- QUANTIFICATION AND STATISTICAL ANALYSIS
  - Analysis of mass spectrometric data and label-free quantification
  - Statistical analysis of proteomic and FACS datasets
  - Functional annotation and downstream data analysis
  - Data analysis of sequencing data (ChIP-Seq)

SUPPLEMENTAL INFORMATION

Supplemental information can be found online at https://doi.org/10.1016/j.celrep.2025.115407.

Received: December 7, 2023
Revised: November 16, 2024
Accepted: February 15, 2025
Published: March 10, 2025

REFERENCES

1. Nam, S., and Lim, J.-S. (2016). Essential role of interferon regulatory factor 4 (IRF4) in immune cell development. Arch Pharm. Res. (Seoul) *39*, 1548–1555. https://doi.org/10.1007/s12272-016-0854-1.
2. Brüstle, A., Heink, S., Huber, M., Rosenplänter, C., Stadelmann, C., Yu, P., Arpaia, E., Mak, T.W., Kamradt, T., and Lohoff, M. (2007). The development of inflammatory TH-17 cells requires interferon-regulatory factor 4. Nat. Immunol. *8*, 958–966. https://doi.org/10.1038/ni1500.
3. Huber, M., and Lohoff, M. (2014). IRF4 at the crossroads of effector T-cell fate decision. Eur. J. Immunol. *44*, 1886–1895. https://doi.org/10.1002/eji.201344279.
4. Lu, J., Liang, T., Li, P., and Yin, Q. (2023). Regulatory effects of IRF4 on immune cells in the tumor microenvironment. Front. Immunol. *14*, 1086803. https://doi.org/10.3389/fimmu.2023.1086803.
5. Ciofani, M., Madar, A., Galan, C., Sellars, M., Mace, K., Pauli, F., Agarwal, A., Huang, W., Parkhurst, C.N., Muratet, M., et al. (2012). A Validated Regulatory Network for Th17 Cell Specification. Cell *151*, 289–303. https://doi.org/10.1016/j.cell.2012.09.016.
6. Li, P., Spolski, R., Liao, W., Wang, L., Murphy, T.L., Murphy, K.M., and Leonard, W.J. (2012). BATF–JUN is critical for IRF4-mediated transcription in T cells. Nature *490*, 543–546. https://doi.org/10.1038/nature11530.
7. Arnold, P.R., Wen, M., Zhang, L., Ying, Y., Xiao, X., Chu, X., Wang, G., Zhang, X., Mao, Z., Zhang, A., et al. (2022). Suppression of FOXP3 expression by the AP-1 family transcription factor BATF3 requires partnering with IRF4. Front. Immunol. *13*, 966364. https://doi.org/10.3389/fimmu.2022.966364.
8. Zheng, Y., Chaudhry, A., Kas, A., deRoos, P., Kim, J.M., Chu, T.-T., Corcoran, L., Treuting, P., Klein, U., and Rudensky, A.Y. (2009). Regulatory T-cell suppressor program co-opts transcription factor IRF4 to control TH2 responses. Nature *458*, 351–356. https://doi.org/10.1038/nature07674.
9. Biswas, P.S., Bhagat, G., and Pernis, A.B. (2010). IRF4 and its regulators: evolving insights into the pathogenesis of inflammatory arthritis? Immunol. Rev. *233*, 79–96. https://doi.org/10.1111/j.0105-2896.2009.00864.x.
10. Alvisi, G., Brummelman, J., Puccio, S., Mazza, E.M., Tomada, E.P., Losurdo, A., Zanon, V., Peano, C., Colombo, F.S., Scarpa, A., et al. (2020). IRF4 instructs effector Treg differentiation and immune suppression in human cancer. J. Clin. Investig. *130*, 3137–3150. https://doi.org/10.1172/JCI130426.
11. Vasanthakumar, A., Liao, Y., Teh, P., Pascutti, M.F., Oja, A.E., Garnham, A.L., Gloury, R., Tempany, J.C., Sidwell, T., Cuadrado, E., et al. (2017). The TNF Receptor Superfamily-NF-κB Axis Is Critical to Maintain Effector Regulatory T Cells in Lymphoid and Non-lymphoid Tissues. Cell Rep. *20*, 2906–2920. https://doi.org/10.1016/j.celrep.2017.08.068.
12. Guo, Z., Xu, P., Ge, S., Zhang, C., Zheng, X., Xu, J., Liu, Z., Li, B., and Ge, S. (2017). Ubiquitin specific peptidase 4 stabilizes interferon regulatory factor protein and promotes its function to facilitate interleukin-4 expression in T helper type 2 cells. Int. J. Mol. Med. *40*, 979–986. https://doi.org/10.3892/ijmm.2017.3087.
13. de Boer, E., Rodriguez, P., Bonte, E., Krijgsveld, J., Katsantoni, E., Heck, A., Grosveld, F., and Strouboulis, J. (2003). Efficient biotinylation and single-step purification of tagged transcription factors in mammalian cells and transgenic mice. Proc. Natl. Acad. Sci. USA *100*, 7480–7485. https://doi.org/10.1073/pnas.1332608100.
14. Driegen, S., Ferreira, R., van Zon, A., Strouboulis, J., Jaegle, M., Grosveld, F., Philipsen, S., and Meijer, D. (2005). A generic tool for biotinylation of tagged proteins in transgenic mice. Transgenic Res. *14*, 477–482.
15. Cai, X., Zhang, W., Hu, J., Zhang, L., Sultana, N., Wu, B., Cai, W., Zhou, B., and Cai, C.L. (2013). Tbx20 acts upstream of Wnt signaling to regulate endocardial cushion formation and valve remodeling during mouse cardiogenesis. Development *140*, 3176–3187. https://doi.org/10.1242/DEV.092502.
16. Chang, C.H., Curtis, J.D., Maggi, L.B., Faubert, B., Villarino, A.V., O'Sullivan, D., Huang, S.C.C., Van Der Windt, G.J.W., Blagih, J., Qiu, J., et al. (2013). Posttranscriptional Control of T Cell Effector Function by Aerobic Glycolysis. Cell *153*, 1239–1251. https://doi.org/10.1016/J.CELL.2013.05.016.
17. Man, K., Miasari, M., Shi, W., Xin, A., Henstridge, D.C., Preston, S., Pellegrini, M., Belz, G.T., Smyth, G.K., Febbraio, M.A., et al. (2013). The transcription factor IRF4 is essential for TCR affinity-mediated metabolic programming and clonal expansion of T cells. Nat. Immunol. *14*, 1155–1165. https://doi.org/10.1038/NI.2710.
18. Gerriets, V.A., Kishton, R.J., Nichols, A.G., Macintyre, A.N., Inoue, M., Ilkayeva, O., Winter, P.S., Liu, X., Priyadharshini, B., Slawinska, M.E., et al. (2015). Metabolic programming and PDHK1 control CD4+ T cell subsets and inflammation. J. Clin. Investig. *125*, 194–207. https://doi.org/10.1172/JCI76012.
19. Kang, M., Lee, H.-S., Choi, J.K., Yu, C.-R., and Egwuagu, C.E. (2021). Deletion of Irf4 in T Cells Suppressed Autoimmune Uveitis and Dysregulated Transcriptional Programs Linked to CD4+ T Cell Differentiation and Metabolism. Int. J. Mol. Sci. *22*, 2775. https://doi.org/10.3390/ijms22052775.
20. Ren, J., Han, L., Tang, J., Liu, Y., Deng, X., Liu, Q., Hao, P., Feng, X., Li, B., Hu, H., and Wang, H. (2019). Foxp1 is critical for the maintenance of regulatory T-cell homeostasis and suppressive function. PLoS Biol. *17*, e3000270. https://doi.org/10.1371/JOURNAL.PBIO.3000270.
21. Kudo-Saito, C., Fuwa, T., and Kawakami, Y. (2016). Targeting ALCAM in the cryo-treated tumour microenvironment successfully induces systemic anti-tumour immunity. Eur. J. Cancer *62*, 54–61. https://doi.org/10.1016/J.EJCA.2016.04.013.
22. de Almeida Nagata, D.E., Ting, H.A., Cavassani, K.A., Schaller, M.A., Mukherjee, S., Ptaschinski, C., Kunkel, S.L., and Lukacs, N.W. (2015). Epigenetic control of Foxp3 by SMYD3 H3K4 histone methyltransferase controls iTreg development and regulates pathogenic T-cell responses during pulmonary viral infection. Mucosal Immunol. *8*, 1131–1143. https://doi.org/10.1038/MI.2015.4/ATTACHMENT/94820189-47C1-4C1E-B850-532379043207/MMC8.PPT.
23. Smith, A.L., Friedman, D.B., Yu, H., Carnahan, R.H., and Reynolds, A.B. (2011). ReCLIP (Reversible Cross-Link Immuno-Precipitation): An efficient method for interrogation of labile protein complexes. PLoS One *6*, e16206. https://doi.org/10.1371/journal.pone.0016206.
24. Ochiai, K., Kondo, H., Okamura, Y., Shima, H., Kurokochi, Y., Kimura, K., Funayama, R., Nagashima, T., Nakayama, K., Yui, K., et al. (2018). Zinc finger-IRF composite elements bound by Ikaros/IRF4 complexes function as gene repression in plasma cell. Blood Adv. *2*, 883–894. https://doi.org/10.1182/bloodadvances.2017010413.
25. Yang, X.O., Panopoulos, A.D., Nurieva, R., Chang, S.H., Wang, D., Watowich, S.S., and Dong, C. (2007). STAT3 regulates cytokine-mediated generation of inflammatory helper T cells. J. Biol. Chem. *282*, 9358–9363. https://doi.org/10.1074/jbc.C600321200.
26. Yang, W.C., Hwang, Y.S., Chen, Y.Y., Liu, C.L., Shen, C.N., Hong, W.H., Lo, S.M., and Shen, C.R. (2017). Interleukin-4 Supports the Suppressive Immune Responses Elicited by Regulatory T Cells. Front. Immunol. *8*, 1508. https://doi.org/10.3389/FIMMU.2017.01508.
27. Ouyang, X., Zhang, R., Yang, J., Li, Q., Qin, L., Zhu, C., Liu, J., Ning, H., Shin, M.S., Gupta, M., et al. (2011). Transcription factor IRF8 directs a silencing programme for TH17 cell differentiation. Nat. Commun. *2*, 314. https://doi.org/10.1038/ncomms1311.

28. Yasuda, K., Kitagawa, Y., Kawakami, R., Isaka, Y., Watanabe, H., Kondoh, G., Kohwi-Shigematsu, T., Sakaguchi, S., and Hirota, K. (2019). Satb1 regulates the effector program of encephalitogenic tissue Th17 cells in chronic inflammation. Nat. Commun. *10*, 549. https://doi.org/10.1038/s41467-019-08404-w.

29. Cho, J.J., Xu, Z., Parthasarathy, U., Drashansky, T.T., Helm, E.Y., Zuniga, A.N., Lorentsen, K.J., Mansouri, S., Cho, J.Y., Edelmann, M.J., et al. (2019). Hectd3 promotes pathogenic Th17 lineage through Stat3 activation and Malt1 signaling in neuroinflammation. Nat. Commun. *10*, 701. https://doi.org/10.1038/s41467-019-08605-3.

30. Wang, X., Ni, L., Chang, D., Lu, H., Jiang, Y., Kim, B.S., Wang, A., Liu, X., Zhong, B., Yang, X., and Dong, C. (2017). Cyclic AMP-Responsive Element-Binding Protein (CREB) is Critical in Autoimmunity by Promoting Th17 but Inhibiting Treg Cell Differentiation. EBioMedicine *25*, 165–174. https://doi.org/10.1016/j.ebiom.2017.10.010.

31. Li, P., Spolski, R., Liao, W., and Leonard, W.J. (2014). Complex interactions of transcription factors in mediating cytokine biology in T cells. Immunol. Rev. *261*, 141–156. https://doi.org/10.1111/imr.12199.

32. Hasan, Z., Koizumi, S.I., Sasaki, D., Yamada, H., Arakaki, N., Fujihara, Y., Okitsu, S., Shirahata, H., and Ishikawa, H. (2017). JunB is essential for IL-23-dependent pathogenicity of Th17 cells. Nat. Commun. *8*, 15628–15712. https://doi.org/10.1038/ncomms15628.

33. Schnell, A., Huang, L., Singer, M., Singaraju, A., Barilla, R.M., Regan, B.M.L., Bollhagen, A., Thakore, P.I., Dionne, D., Delorey, T.M., et al. (2021). Stem-like intestinal Th17 cells give rise to pathogenic effector T cells during autoimmunity. Cell *184*, 6281–6298.e23. https://doi.org/10.1016/J.CELL.2021.11.018.

34. Bowers, J.S., Nelson, M.H., Majchrzak, K., Bailey, S.R., Rohrer, B., Kaiser, A.D., Atkinson, C., Gattinoni, L., and Paulos, C.M. (2017). Th17 cells are refractory to senescence and retain robust antitumor activity after long-term ex vivo expansion. JCI Insight *2*, e90772. https://doi.org/10.1172/JCI.INSIGHT.90772.

35. van der Veeken, J., Glasner, A., Zhong, Y., Hu, W., Wang, Z.-M., Bou-Puerto, R., Charbonnier, L.-M., Chatila, T.A., Leslie, C.S., and Rudensky, A.Y. (2020). The Transcription Factor Foxp3 Shapes Regulatory T Cell Identity by Tuning the Activity of trans-Acting Intermediaries. Immunity *53*, 971–984.e5. https://doi.org/10.1016/j.immuni.2020.10.010.

36. Sidwell, T., Liao, Y., Garnham, A.L., Vasanthakumar, A., Gloury, R., Blume, J., Teh, P.P., Chisanga, D., Thelemann, C., de Labastida Rivera, F., et al. (2020). Attenuation of TCR-induced transcription by Bach2 controls regulatory T cell differentiation and homeostasis. Nat. Commun. *11*, 252–317. https://doi.org/10.1038/s41467-019-14112-2.

37. Wang, Z., Wang, P., Li, Y., Peng, H., Zhu, Y., Mohandas, N., and Liu, J. (2021). Interplay between Cofactors and Transcription Factors in Hematopoiesis and Hematological Malignancies. Signal Transduct Target Ther. *6*, 24. https://doi.org/10.1038/s41392-020-00422-1.

38. Oestreich, K.J., and Weinmann, A.S. (2012). Ikaros changes the face of NuRD remodeling. Nat. Immunol. *13*, 16–18. https://doi.org/10.1038/ni.2191.

39. Naito, T., Gómez-del Arco, P., Williams, C.J., and Georgopoulos, K. (2007). Antagonistic Interactions between Ikaros and the Chromatin Remodeler Mi-2β Determine Silencer Activity and Cd4 Gene Expression. Immunity *27*, 723–734. https://doi.org/10.1016/j.immuni.2007.09.008.

40. Morawski, P.A., Mehra, P., Chen, C., Bhatti, T., and Wells, A.D. (2013). Foxp3 protein stability is regulated by cyclin-dependent kinase 2. J. Biol. Chem. *288*, 24494–24502. https://doi.org/10.1074/JBC.M113.467704.

41. Gao, T., and Qian, J. (2020). EnhancerAtlas 2.0: an updated resource with enhancer annotation in 586 tissue/cell types across nine species. Nucleic Acids Res. *48*, D58–D64. https://doi.org/10.1093/nar/gkz980.

42. Zeng, W., Chen, S., Cui, X., Chen, X., Gao, Z., and Jiang, R. (2021). SilencerDB: a comprehensive database of silencers. Nucleic Acids Res. *49*, D221–D228. https://doi.org/10.1093/nar/gkaa839.

43. Kel, A.E., Gössling, E., Reuter, I., Cheremushkin, E., Kel-Margoulis, O.V., and Wingender, E. (2003). MATCHTM: a tool for searching transcription factor binding sites in DNA sequences. Nucleic Acids Res. *31*, 3576–3579. https://doi.org/10.1093/nar/gkg585.

44. Matys, V., Kel-Margoulis, O.V., Fricke, E., Liebich, I., Land, S., Barre-Dirrie, A., Reuter, I., Chekmenev, D., Krull, M., Hornischer, K., et al. (2006). TRANSFAC(R) and its module TRANSCompel(R): transcriptional gene regulation in eukaryotes. Nucleic Acids Res. *34*, D108–D110. https://doi.org/10.1093/nar/gkj143.

45. Machanick, P., and Bailey, T.L. (2011). MEME-ChIP: motif analysis of large DNA datasets. Bioinformatics *27*, 1696–1697. https://doi.org/10.1093/bioinformatics/btr189.

46. Bailey, T.L., Boden, M., Buske, F.A., Frith, M., Grant, C.E., Clementi, L., Ren, J., Li, W.W., and Noble, W.S. (2009). MEME SUITE: tools for motif discovery and searching. Nucleic Acids Res. *37*, W202–W208. https://doi.org/10.1093/nar/gkp335.

47. Gupta, S., Stamatoyannopoulos, J.A., Bailey, T.L., and Noble, W.S. (2007). Quantifying similarity between motifs. Genome Biol. *8*, R24. https://doi.org/10.1186/gb-2007-8-2-r24.

48. Glasmacher, E., Agrawal, S., Chang, A.B., Murphy, T.L., Zeng, W., Vander Lugt, B., Khan, A.A., Ciofani, M., Spooner, C.J., Rutz, S., et al. (2012). A Genomic Regulatory Element That Directs Assembly and Function of Immune-Specific AP-1–IRF Complexes. Science *338*, 975–980. https://doi.org/10.1126/science.1228309.

49. Cook, S.L., Franke, M.C., Sievert, E.P., and Sciammas, R. (2020). A synchronous IRF4-dependent gene regulatory network in B and Th cellsorchestrating the antibody response. Trends Immunol. *41*, 614–628. https://doi.org/10.1016/J.IT.2020.05.001.

50. Trepte, P., Kruse, S., Kostova, S., Hoffmann, S., Buntru, A., Tempelmeier, A., Secker, C., Diez, L., Schulz, A., Klockmeier, K., et al. (2018). Lu TH y: a double-readout bioluminescence-based two-hybrid technology for quantitative mapping of protein–protein interactions in mammalian cells. Mol. Syst. Biol. *14*, e8071. https://doi.org/10.15252/MSB.20178071/SUPPL_FILE/MSB178071-SUP-0013-DATASETEV12.XLSX.

51. Ravasi, T., Suzuki, H., Cannistraci, C.V., Katayama, S., Bajic, V.B., Tan, K., Akalin, A., Schmeier, S., Kanamori-Katayama, M., Bertin, N., et al. (2010). An atlas of combinatorial transcriptional regulation in mouse and man. Cell *140*, 744–752. https://doi.org/10.1016/J.CELL.2010.01.044.

52. Hsieh, J.Y., Chen, K.C., Wang, C.H., Liu, G.Y., Ye, J.A., Chou, Y.T., Lin, Y.C., Lyu, C.J., Chang, R.Y., Liu, Y.L., et al. (2023). Suppression of the human malic enzyme 2 modifies energy metabolism and inhibits cellular respiration. Commun. Biol. *6*, 548. https://doi.org/10.1038/s42003-023-04930-y.

53. Ni, X., Kou, W., Gu, J., Wei, P., Wu, X., Peng, H., Tao, J., Yan, W., Yang, X., Lebid, A., et al. (2019). TRAF6 directs FOXP3 localization and facilitates regulatory T-cell function through K63-linked ubiquitination. EMBO J. *38*, e99766. https://doi.org/10.15252/EMBJ.201899766.

54. Schutt, S.D., Wu, Y., Kharel, A., Bastian, D., Choi, H.-J., Hanief Sofi, M., Mealer, C., McDaniel Mims, B., Nguyen, H., Liu, C., et al. (2022). The druggable transcription factor Fli-1 regulates T cell immunity and tolerance in graft-versus-host disease. J. Clin. Investig. *132*, e143950. https://doi.org/10.1172/JCI143950.

55. Kober, C., Roewe, J., Schmees, N., Roese, L., Roehn, U., Bader, B., Stoeckigt, D., Prinz, F., Gorjánácz, M., Roider, H.G., et al. (2023). Targeting the aryl hydrocarbon receptor (AhR) with BAY 2416964: a selective small molecule inhibitor for cancer immunotherapy. J. Immunother. Cancer *11*, e007495. https://doi.org/10.1136/JITC-2023-007495.

56. Cheng, J., Wang, S., Lv, S.Q., Song, Y., and Guo, N.H. (2023). Resveratrol inhibits AhR/Notch axis and reverses Th17/Treg imbalance in purpura by activating Foxp3. Toxicol. Res. *12*, 381–391. https://doi.org/10.1093/TOXRES/TFAD021.

57. Rosenbauer, F., Waring, J.F., Foerster, J., Wietstruk, M., Philipp, D., and Horak, I. (1999). Interferon consensus sequence binding protein and interferon regulatory factor-4/Pip form a complex that represses the

expression of the interferon-stimulated gene-15 in macrophages. Blood *94*, 4274–4281.

58. Kwon, H., Thierry-Mieg, D., Thierry-Mieg, J., Kim, H.-P., Oh, J., Tunyaplin, C., Carotta, S., Donovan, C.E., Goldman, M.L., Tailor, P., et al. (2009). Analysis of Interleukin-21-Induced Prdm1 Gene Regulation Reveals Functional Cooperation of STAT3 and IRF4 Transcription Factors. Immunity *31*, 941–952. https://doi.org/10.1016/j.immuni.2009.10.008.

59. Wang, X., Lennard Richard, M., Li, P., Henry, B., Schutt, S., Yu, X.-Z., Fan, H., Zhang, W., Gilkeson, G., and Zhang, X.K. (2021). Expression of GM-CSF Is Regulated by Fli-1 Transcription Factor, a Potential Drug Target. J. Immunol. *206*, 59–66. https://doi.org/10.4049/jimmunol.2000664.

60. Schutt, S.D., Bastian, D., Choi, H.-J., Wu, Y., Sofi, M.H., Nguyen, H., Zhang, X., and Yu, X.-Z. (2019). Fli-1 Regulates Multiple T-Cell Subsets during Inflammatory Responses and Experimental Graft-Versus-Host Disease. Blood *134*, 3201. https://doi.org/10.1182/blood-2019-127577.

61. Sundararaj, K.P., Thiyagarajan, T., Molano, I., Basher, F., Powers, T.W., Drake, R.R., and Nowling, T.K. (2015). FLI1 Levels Impact CXCR3 Expression and Renal Infiltration of T Cells and Renal Glycosphingolipid Metabolism in the MRL/lpr Lupus Mouse Strain. J. Immunol. *195*, 5551–5560. https://doi.org/10.4049/jimmunol.1500961.

62. Beyer, M., Thabet, Y., Müller, R.U., Sadlon, T., Classen, S., Lahl, K., Basu, S., Zhou, X., Bailey-Bucktrout, S.L., Krebs, W., et al. (2011). Repression of the genome organizer SATB1 in regulatory T cells is required for suppressive function and inhibition of effector differentiation. Nat. Immunol. *12*, 898–907. https://doi.org/10.1038/ni.2084.

63. Okuda, S., Watanabe, Y., Moriya, Y., Kawano, S., Yamamoto, T., Matsumoto, M., Takami, T., Kobayashi, D., Araki, N., Yoshizawa, A.C., et al. (2017). jPOSTrepo: an international standard data repository for proteomes. Nucleic Acids Res. *45*, D1107–D1111. https://doi.org/10.1093/NAR/GKW1080.

64. Klein, U., Casola, S., Cattoretti, G., Shen, Q., Lia, M., Mo, T., Ludwig, T., Rajewsky, K., and Dalla-Favera, R. (2006). Transcription factor IRF4 controls plasma cell differentiation and class-switch recombination. Nat. Immunol. *7*, 773–782. https://doi.org/10.1038/ni1357.

65. Albrecht, S., Sprang, M., Andrade-Navarro, M.A., and Fontaine, J.-F. (2021). seqQscorer: automated quality control of next-generation sequencing data using machine learning. Genome Biol. *22*, 75. https://doi.org/10.1186/s13059-021-02294-2.

66. Lerdrup, M., Johansen, J.V., Agrawal-Singh, S., and Hansen, K. (2016). An interactive environment for agile analysis and visualization of ChIP-sequencing data. Nat. Struct. Mol. Biol. *23*, 349–357. https://doi.org/10.1038/nsmb.3180.

67. Demichev, V., Messner, C.B., Vernardis, S.I., Lilley, K.S., and Ralser, M. (2020). DIA-NN: neural networks and interference correction enable deep proteome coverage in high throughput. Nat. Methods *17*, 41–44. https://doi.org/10.1038/s41592-019-0638-x.

68. Mi, H., Muruganujan, A., Ebert, D., Huang, X., and Thomas, P.D. (2019). PANTHER version 14: more genomes, a new PANTHER GO-slim and improvements in enrichment analysis tools. Nucleic Acids Res. *47*, D419–D426. https://doi.org/10.1093/nar/gky1038.

69. Shannon, P., Markiel, A., Ozier, O., Baliga, N.S., Wang, J.T., Ramage, D., Amin, N., Schwikowski, B., and Ideker, T. (2003). Cytoscape: A Software Environment for Integrated Models of Biomolecular Interaction Networks. Genome Res. *13*, 2498–2504. https://doi.org/10.1101/gr.1239303.

70. Szklarczyk, D., Gable, A.L., Lyon, D., Junge, A., Wyder, S., Huerta-Cepas, J., Simonovic, M., Doncheva, N.T., Morris, J.H., Bork, P., et al. (2019). STRING v11: protein–protein association networks with increased coverage, supporting functional discovery in genome-wide experimental datasets. Nucleic Acids Res. *47*, D607–D613. https://doi.org/10.1093/nar/gky1131.

71. Yu, G., Wang, L.-G., and He, Q.-Y. (2015). ChIPseeker: an R/Bioconductor package for ChIP peak annotation, comparison and visualization. Bioinformatics *31*, 2382–2383. https://doi.org/10.1093/bioinformatics/btv145.

72. Zhu, L.J., Gazin, C., Lawson, N.D., Pagès, H., Lin, S.M., Lapointe, D.S., and Green, M.R. (2010). ChIPpeakAnno: a Bioconductor package to annotate ChIP-seq and ChIP-chip data. BMC Bioinf. *11*, 237. https://doi.org/10.1186/1471-2105-11-237.

73. Lee, P.P., Fitzpatrick, D.R., Beard, C., Jessup, H.K., Lehar, S., Makar, K.W., Pérez-Melgosa, M., Sweetser, M.T., Schlissel, M.S., Nguyen, S., et al. (2001). A Critical Role for Dnmt1 and DNA Methylation in T Cell Development, Function, and Survival. Immunity *15*, 763–774. https://doi.org/10.1016/S1074-7613(01)00227-8.

74. Ulges, A., Witsch, E.J., Pramanik, G., Klein, M., Birkner, K., Bühler, U., Wasser, B., Luessi, F., Stergiou, N., Dietzen, S., et al. (2016). Protein kinase CK2 governs the molecular decision between encephalitogenic T_H 17 cell and T_{reg} cell development. Proc. Natl. Acad. Sci. USA *113*, 10145–10150. https://doi.org/10.1073/pnas.1523869113.

75. Larochelle, C., Cayrol, R., Kebir, H., Alvarez, J.I., Lécuyer, M.A., Ifergan, I., Viel, É., Bourbonnière, L., Beauseigle, D., Terouz, S., et al. (2012). Melanoma cell adhesion molecule identifies encephalitogenic T lymphocytes and promotes their recruitment to the central nervous system. Brain *135*, 2906–2924. https://doi.org/10.1093/brain/aws212.

76. Sielaff, M., Kuharev, J., Bohn, T., Hahlbrock, J., Bopp, T., Tenzer, S., and Distler, U. (2017). Evaluation of FASP, SP3, and iST Protocols for Proteomic Sample Preparation in the Low Microgram Range. J. Proteome Res. *16*, 4060–4072. https://doi.org/10.1021/acs.jproteome.7b00433.

77. Hughes, C.S., Foehr, S., Garfield, D.A., Furlong, E.E., Steinmetz, L.M., and Krijgsveld, J. (2014). Ultrasensitive proteome analysis using paramagnetic bead technology. Mol. Syst. Biol. *10*, 757. https://doi.org/10.15252/msb.20145625.

78. Distler, U., Kuharev, J., Navarro, P., and Tenzer, S. (2016). Label-free quantification in ion mobility–enhanced data-independent acquisition proteomics. Nat. Protoc. *11*, 795–812. https://doi.org/10.1038/nprot.2016.042.

79. Hahne, H., Pachl, F., Ruprecht, B., Maier, S.K., Klaeger, S., Helm, D., Médard, G., Wilm, M., Lemeer, S., and Kuster, B. (2013). DMSO enhances electrospray response, boosting sensitivity of proteomic experiments. Nat. Methods *10*, 989–991. https://doi.org/10.1038/nmeth.2610.

80. Distler, U., Kuharev, J., Navarro, P., Levin, Y., Schild, H., and Tenzer, S. (2014). Drift time-specific collision energies enable deep-coverage data-independent acquisition proteomics. Nat. Methods *11*, 167–170. https://doi.org/10.1038/nmeth.2767.

81. Meier, F., Brunner, A.D., Frank, M., Ha, A., Bludau, I., Voytik, E., Kaspar-Schoenefeld, S., Lubeck, M., Raether, O., Bache, N., et al. (2020). diaPASEF: parallel accumulation-serial fragmentation combined with data-independent acquisition. Nat. Methods *17*, 1229–1236. https://doi.org/10.1038/S41592-020-00998-0.

82. Wiemann, S., Pennacchio, C., Hu, Y., Hunter, P., Harbers, M., Amiet, A., Bethel, G., Busse, M., Carninci, P., Diekhans, M., et al. (2016). The ORFeome Collaboration: a genome-scale human ORF-clone resource. Nat. Methods *13*, 191–192. https://doi.org/10.1038/NMETH.3776.

83. Silva, J.C., Gorenstein, M.V., Li, G.-Z., Vissers, J.P.C., and Geromanos, S.J. (2006). Absolute quantification of proteins by LCMSE: a virtue of parallel MS acquisition. Mol. Cell. Proteomics *5*, 144–156. https://doi.org/10.1074/mcp.M500230-MCP200.

84. Ritchie, M.E., Phipson, B., Wu, D., Hu, Y., Law, C.W., Shi, W., and Smyth, G.K. (2015). limma powers differential expression analyses for RNA-sequencing and microarray studies. Nucleic Acids Res. *43*, e47. https://doi.org/10.1093/nar/gkv007.

85. Zhang, X., Smits, A.H., van Tilburg, G.B., Ovaa, H., Huber, W., and Vermeulen, M. (2018). Proteome-wide identification of ubiquitin interactions using UbIA-MS. Nat. Protoc. *13*, 530–550. https://doi.org/10.1038/nprot.2017.147.

86. Lê, S., Josse, J., and Husson, F. (2008). **FactoMineR** : An *R* Package for Multivariate Analysis. J. Stat. Software *25*, 1–18. https://doi.org/10.18637/jss.v025.i01.

87. Kolde; Raivo (2012). Pheatmap: pretty heatmaps. R package version *1*, 726.

88. Wickham, H. (2016). ggplot2: Elegant Graphics for Data Analysis (Springer-Verlag).

89. Wu, T., Hu, E., Xu, S., Chen, M., Guo, P., Dai, Z., Feng, T., Zhou, L., Tang, W., Zhan, L., et al. (2021). clusterProfiler 4.0: A universal enrichment tool for interpreting omics data. Innovation *2*, 100141. https://doi.org/10.1016/j.xinn.2021.100141.

90. Doncheva, N.T., Morris, J.H., Gorodkin, J., and Jensen, L.J. (2019). Cytoscape StringApp: Network Analysis and Visualization of Proteomics Data. J. Proteome Res. *18*, 623–632. https://doi.org/10.1021/acs.jproteome.8b00702.

STAR★METHODS

KEY RESOURCES TABLE

REAGENT or RESOURCE	SOURCE	IDENTIFIER
Antibodies		
Brilliant violet 711-conjugated rat anti-mouse CD4; clone GK1.5	BD Biosciences	Cat#: 563050; RRID:AB_2737973
Phycoerythrin-conjugated rat anti-mouse CD62L; clone MEL-14	BioLegend	Cat#: 104407; RRID:AB_313094
Brilliant violet 605-conjugated rat anti-mouse/human CD44; clone IM7	BioLegend	Cat#: 103047; RRID:AB_2562451
Allophycocyanin-conjugated rat anti-mouse/human RORγt; clone AFKJS-9	Thermo Fisher Scientific	Cat#: 17-6988-82; RRID:AB_10609207
Phycoerythrin-conjugated rat anti-mouse IL-17A; clone eBio17B7	Thermo Fisher Scientific	Cat#: 12-7177-81; RRID:AB_763582
Fluorescein isothiocyanate-conjugated rat anti-mouse CD25; clone 3C7	BioLegend	Cat#: 101907; RRID:AB_961210
Phycoerythrin-conjugated rat anti-mouse FOXP3; clone FJK-16s	Thermo Fisher Scientific	Cat#: 12-5773-82; RRID:AB_465936
Phycoerythrin-conjugated rat IgG2a,κ isotype control	Thermo Fisher Scientific	Cat#: 12-4321-80; RRID:AB_1834380
Allophycocyanin-conjugated rat IgG2a,κ isotype control	Thermo Fisher Scientific	Cat#: 17-4321-81; RRID:AB_470181
phycoerythrin-conjugated mouse anti-human/rat CD45RO; clone UCHL1	Thermo Fisher Scientific	Cat#: 12-0457-42; RRID:AB_1272079
phycoerythrin-cyan7-conjugated mouse anti-human MCAM; clone P1H12	BD Biosciences	Cat#: 562135; RRID:AB_10894593
fluorescein-5-isothiocyanate-conjugated mouse anti-human CD4; clone SK3	BD Biosciences	Cat#: 566911; RRID:AB_2739682
Alexa Fluor 700 (AF700)-conjugated mouse anti-human CD3; clone UCHT1	Biolegend	Cat#: 300423; RRID:AB_493740
Horizon-conjugated mouse anti-human CCR6; clone 11A9	BD Biosciences	Cat#: 563704; RRID:AB_2738381
Polyclonal rabbit anti-IRF4 (P173)	Cell Signaling Technology	Cat#: 4948S
Monoclonal mouse anti-IRF4 (F-4, clone sc-48338)	Santa Cruz Biotechnology	Cat#: sc-48338; RRID:AB_627828
Horseradish peroxidase-conjugated anti-rabbit IgG	Cell Signaling Technology	Cat#: 7074P2; RRID:AB_2099233
Horseradish peroxidase-conjugated anti-mouse IgG	Cell Signaling Technology	Cat#: 7076P2; RRID:AB_330924
Phycoerythrin-conjugated rat anti-human/mouse IRF4; clone 3E4	Thermo Fisher Scientific	Cat#: 12-9858-82; RRID:AB_10852721
Phycoerythrin-conjugated rat IgG1κ isotype control	BioLegend	Cat#: 400407; RRID:AB_326513
Allophycocyanin-conjugated rat anti-mouse/human CD4; clone GK1.5	Thermo Fisher Scientific	Cat#: 17-0041-82; RRID:AB_469320
Monoclonal anti-CD3; clone 145-2C11	In house	N/A
Monoclonal anti-CD28; clone 37.51	In house	N/A
Monoclonal anti-IFN-γ; clone XMG1.2	In house	N/A
Monoclonal anti-IL-4; clone 11B11	In house	N/A
Monoclonal anti-α-tubulin; clone GT114	GeneTex	Cat#: GTX628802; RRID: AB_2716636
Polyclonal anti-laminA/C	Cell Signaling Technology	Cat#: 2032S; RRID:AB_2136278
Bacterial and virus strains		
DH5alpha	Thermo Fisher Scientific	Cat#: 18265017
Chemicals, peptides, and recombinant proteins		
TGF-β	Peprotech	Cat#: 17830943
IL-6	Peprotech	Cat#: 216-16
IL-2	In house	N/A
Etoposide	Sigma Aldrich	Cat#: 341205
BAY2416964	Selleckchem	Cat#: S8995
Resveratrol	Selleckchem	Cat#: S1396

(*Continued on next page*)

Continued

REAGENT or RESOURCE	SOURCE	IDENTIFIER
Horseradish peroxidase–conjugated streptavidin	Sigma Aldrich	Cat#: 11089153001
eBioscience Fixable Viability Dye eFlour780	Thermo Fisher Scientific	Cat#: 65-0865-14
Bovine Serum Albumin (BSA)	Sigma-Aldrich	Cat#: A8412
Phorbol Myristate Acetate (PMA)	Thermo Fisher Scientific	Cat#: J63916.MCR
Dithiobis[succinimidyl propionate] (DSP)	Thermo Fisher Scientific	Cat#: 22585
cComplete™ Protease Inhibitor Cocktail	Roche	Cat#: 11697498001
EDTA	Carl Roth	Cat#: 8043.2
Dimethyl sulphoxide (DMSO) ROTISOLV® ≥99,99 %, Headspace Grade	Carl Roth	Cat#: HN47.1
Magnesium Chlorde (MgCl2)	Carl Roth	Cat#: KK36.1
Sodium chloride (NaCl) ≥99,5 %, p.a., ACS, ISO	Carl Roth	Cat#: 3957.2
Igepal CA-630	Sigma Aldrich	Cat#: I8896-100ML
Sodium deoxycholate	Merck	Cat#: 30970-25G
Sodium Dodecyl Sulfate (SDS)	Carl Roth	Cat#: 8029.4
Tris PUFFERAN® ≥99,9 %, p.a.	Carl Roth	Cat#: 4855.2
TRIS hydrochloride PUFFERAN® ≥99,9 %, p.a.	Carl Roth	Cat#: 9090.3
Biotin	Sigma Aldrich	Cat#: B4501-1G
Iodoacetamid (IAA) BioUltra	Sigma-Aldrich	Cat#: I1149-5G
1,4-Dithiothreitol (DTT) ≥99 %, p.a.	Carl Roth	Cat#: 6908.1
Ammonium hydrogen carbonate (AMBIC) ≥99 %, p.a.	Carl Roth	Cat#: T871.1
Tween 20	PanReac AppliChem	Cat#: A4974
Sodium pyruvate	Carl Roth	Cat#: 9182.1
Pierce 16 % Formaldehyde, methanol-free	ThermoFisher	Cat#: 28906
Triton X-100Carl RothCat#: 3051.2Lithium Chloride (LiCl)	Carl Roth	Cat#: 3739.1
RNAse A (10 mg/mL)	Thermo Fisher Scientific	Cat#: EN0531
Proteinase K (from Tritirachium album)	Serva	Cat#: 33755.01
HoechstImmunoChemistry TechnologiesCat#: ICT-639Mowiol	In house	N/A
eBioscoence Monensin-Lösung (1,000x)InvitrogenCat#: 00-4505-51Ionomycin (from Streptomyces conglobatus)	Sigma-Aldrich	Cat#: I9657
Fixation/Permeabilization Concentrate	Invitrogen	Cat#: 00-5123-43
Fixation/Permeabilization Diluent	Invitrogen	Cat#: 00-5223-56
10x Permeabilization Buffer	Invitrogen	Cat#: 12766048
Roti-PreMix PBS	Carl Roth	Cat#: 0890.1
Trypsin Gold, Mass Spectrometry Grade	Promega	Cat#: V5280
IMDM, w/o: L-Glutamine, w: 3.024 g/L NaHCO3	PAN Biotech	Cat#: P04-20250
Fetal calf serum (FCS)	Thermo Fisher Scientific	Cat#: A5670701
Nuclease-free water	QIAGEN	Cat#: 0890.1
ROTISOLV® Acetonitrile ≥99,98 %, Ultra LC-MS	Carl Roth	Cat#: HN40.1
ROTISOLV® water, Ultra LC-MS	Carl Roth	Cat#: HN43.1
Ethanol (pure)	PanReac AppliChem	Cat#: 141086.1211
Formic acid ROTIPURAN® ≥99 %, LC-MS Grade	Carl Roth	Cat#: 1EHK.1
PageRuler™ Plus Prestained Protein Ladder, 10 to 250 kDa	Thermo Fisher Scientific	Cat#: 26619
Gateway™ LR Clonase™ II Enzym-Mix	Thermo Fisher Scientific	Cat#: 11791020
Lipofectamine™ 2000	Thermo Fisher Scientific	Cat#: 11668019
h-Coelenterazine (Benzyl-)	PJK Biotech	Cat#: 102181
Critical commercial assays		
Naïve $CD4^+$ T Cell Isolation Kit, mouse	Miltenyi Biotec	Cat#: 130-104-453
$CD4^+$ T Cell Isolation Kit, human	Miltenyi Biotec	Cat#: 130-096-533

(*Continued on next page*)

Continued

REAGENT or RESOURCE	SOURCE	IDENTIFIER
DNA Clean & Concentrator	Zymo	Cat#: D4014
NEBNext Ultra II DNA Library Prep Kit	Illumina	Cat#: E7645L
Qubit® dsDNA HS Assay Kit	Thermo Fisher Scientific	Cat#: Q32851
Trans-Blot® Turbo™ RTA Transfer Kit, PVDF	BioRad	Cat#: #1704274
Western Bright Chemiluminescence Substrate	Biozym	Cat#: 541004
μMACS FactorFinder Kit	Miltenyi Biotec	Cat#: 130-074-101
7.5% Mini-PROTEAN® TGX™ Precast Protein Gels, 10-well, 50 μl	BioRad	Cat#: 4561024
Deposited data		
Mass spectrometry proteomics data	ProteomeXChange/jPOST	PXD044298/ JPST002260 (murine data) and PXD060137/JPST003563 (human data)
IRF4 ChIP-seq data	NCBI GEO	GSE240979
R scripts used for statistical analysis	Github/Zenodo	https://github.com/Muedi/IRF4-in-Treg-and-Th17; https://doi.org/10.5281/zenodo.14643315
Experimental models: Cell lines		
HEK293	DSMZ	Cat#: ACC-no.305
Experimental models: Organisms/strains		
BAC transgenic mice; strain C57BL/6J-*Irf4*^{em1Bopp}	Cyagen US Inc.	N/A
ROSA26^{BirA} mice; strain *Gt(ROSA)26*$^{Sortm1.1(birA)Mejr}$	Großfeld and Klein-Heßling lab	N/A
IRF4^{Bio} mice; strain C57BL/6J-*Irf4*^{em1Bopp} *Gt(ROSA)26*$^{Sortm1.1(birA)Mejr}$	This paper	N/A
CD4^{Cre}xIRF4$^{fl/fl}$ mice	Klein et al.[64]	N/A
Oligonucleotides		
IL-10 fwd: 5'AATCCGAGAAACCCACCA3'	Sigma Aldrich	N/A
IL-10 rev: 5' TCCATACCAAAACCCCAG3'	Sigma Aldrich	N/A
Ezh2 fwd: 5'CTTCTCAACCCCTTTCCCTAAGA3'	Sigma Aldrich	N/A
Ezh2 rev: 5'CACCTTATTCCCAAAGGCAAGG3'	Sigma Aldrich	N/A
pENT_fwd: 5'TTGTAAAACGACGGCCAGTC3'	Sigma Aldrich	N/A
pENT_rev: 5'GCCAGGAAACAGCTATGACC3'	Sigma Aldrich	N/A
NanoLuc-398fwd: 5'GAACGGCAACAAAATTATCGAC3'	Sigma Aldrich	N/A
NanoLuc-109rev: 5'CCCCGAGATTCTGAAACAAAC3'	Sigma Aldrich	N/A
mCitrine-131rev: 5'AGTGTGAGTTTCCCATATGTCG3'	Sigma Aldrich	N/A
mCitrine-547fwd: 5'AGCAGAATACGCCCATCG3'	Sigma Aldrich	N/A
pEXP_rev: 5'GGCAACTAGAAGGCACAGTC3'	Sigma Aldrich	N/A
pEXP_fwd: 5'GGCTAACTAGAGAACCCACTG3'	Sigma Aldrich	N/A
Recombinant DNA		
pcDNA3.1	ThermoFisher	Cat#: V79020
pcDNA3.1-cmyc-NL	Addgene	Plasmid ID: 113442
pcDNA3.1-PA-mCit	Addgene	Plasmid ID: 113443
pcDNA3.-cmyc-NL-GW	Addgene	Plasmid ID: 113446
pcDNA3.1-GW-NL-cmyc	Addgene	Plasmid ID: 113447
pcDNA3.1-GW-mCit	Trepte et al.[50]	N/A
pcDNA3.1-mCit-GW	Trepte et al. [50]	N/A
pcDNA3.1-GW-His3C-mCit	This study	N/A
pcDNA3.1-mCit-His3C-GW	This study	N/A

(*Continued on next page*)

Continued

REAGENT or RESOURCE	SOURCE	IDENTIFIER
pcDNA3.1 cmyc-NL-IRF4	This study	N/A
pcDNA3.1 IRF4-NL-cmyc		
pcDNA3.1 mCit-His3C-IRF4		
pcDNA3.1 IRF4-mCit		
pcDNA3.1 cmyc-NL-FLI1		
pcDNA3.1 FLI1-NL-cmyc		
pcDNA3.1 mCit-His3C-FLI1		
pcDNA3.1 FLI1-His3C-mCit		
pcDNA3.1 mCit-His3C-BACH2		
pcDNA3.1 BACH2-His3C-mCit		
pcDNA3.1 mCit-His3C-BATF		
pcDNA3.1 BATF-His3C-mCit		
pcDNA3.1 cmyc-NL-ETV6		
pcDNA3.1 mCit-His3C-ETV6		
pcDNA3.1 ETV6-His3C-mCit		
pcDNA3.1 cmyc-NL-ETV7		
pcDNA3.1 ETV7-NL-cmyc		
pcDNA3.1 mCit-His3C-ETV7		
pcDNA3.1 ETV7-His3C-mCit		
pcDNA3.1 mCit-His3C-FOSL2		
pcDNA3.1 mCit-His3C-FOXP3		
pcDNA3.1 cmyc-NL-GIPC2		
pcDNA3.1 mCit-His3C-GIPC2		
pcDNA3.1 GIPC2-His3C-mCit		
pcDNA3.1 cmyc-NL-HMMR		
pcDNA3.1 HMMR-NL-cmyc		
pcDNA3.1 mCit-His3C-IRF8		
pcDNA3.1 IRF8-His3C-mCit		
pcDNA3.1 cmyc-NL-RNF40		
pcDNA3.1 RNF40-NL-cmyc		
pcDNA3.1 mCit-His3C-RNF40		
pcDNA3.1 RNF40-His3C-mCit		
pcDNA3.1 SATB1-NL-cmyc		
pcDNA3.1 SPI1-NL-cmyc		
pcDNA3.1 mCit-His3C-SPI1		
pcDNA3.1 SPI1-His3C-mCit		
Software and algorithms		
FACSDiva, version 6.1.3	BD	N/A
FlowJo, version 10	BD	N/A
seqQscorer	Albrecht et al.[65]	https://github.com/salbrec/seqQscorer
EaSeq, version 1.2	Lerdrup et al.[66]	https://easeq.net
Quantity One, version 4.4.0	BioRad	N/A
Imaris, version 9.3.1	BitPlane	N/A
ISOQuant, version 1.8	in-house	https://github.com/jkuharev/ISOQuant
DIA-NN, version 1.7.13	Demichev et al.[67]	https://github.com/vdemichev/DiaNN
PANTHER, version 14.0	Mi et al.[68]	http://geneontology.org/
Cytoscape, version 3.8.0	Shannon et al.[69]	https://cytoscape.org/
STRING DB, version 11	Szklarczyk et al.[70]	https://string-db.org/
Venny web application		http://bioinfogp.cnb.csic.es/tools/venny/index.html
R studio		https://cran.r-project.org/
ChIPseeker	Yu et al.[71]	https://guangchuangyu.github.io/software/ChIPseeker/
UCSCs LiftOver		https://genome.ucsc.edu/cgi-bin/hgLiftOver

(*Continued on next page*)

Continued

REAGENT or RESOURCE	SOURCE	IDENTIFIER
ChIPPeakAnno	Zhu et al.[72]	https://github.com/jianhong/ChIPpeakAnno
MEME suite		https://meme-suite.org/meme/
Tecan i-control 2.0.10.0	Tecan	N/A
GraphPad Prism, version 10.3.1	GraphPad Software	https://www.graphpad.com
Other		
Dynabeads™ M-280	Thermo Fisher Scientific	Cat#: 11205D
Sera-Mag™ Carboxylate-Modified Magnetic Beads & SpeedBeads	Cytiva	Cat#: 65152105050250 Cat#: 45152105050250
PVFD membrane (0.45 μm pore size)	Thermo Fisher Scientific	Cat#: 88518
TXP microtubes	Diagenode	Cat#: C30010010-300
LS Columns	Miltenyi Biotec	Cat#: 130-042-401

EXPERIMENTAL MODEL AND STUDY PARTICIPANT DETAILS

Animals

Bacterial artificial chromosome (BAC) transgenic mice (C57BL/6J-*Irf4*^{em1Bopp}, referred to as IRF4$^{Avi\text{-}tag}$ mice in the manuscript) were ordered from Cyagen US Inc. (Santa Clara, CA, USA). Detailed information on the IRF4$^{Avi\text{-}tag}$ mouse strain expressing a fusion protein of IRF4 and the BirA recognition site (Avi-tag) under the control of the endogenous *Irf4* promotor is provided in Figure S5. IRF4$^{Avi\text{-}tag}$ mice were cross-bred with the ROSA26^{BirA} (*Gt(ROSA)26*$^{Sortm1.1(birA)Mejr}$) mouse strain ubiquitously expressing BirA ligase under the Rosa26 promotor.[14] ROSA26^{BirA} mice were kindly provided by Frank Großfeld/Dr. S. Klein-Heßling (Marburg, Germany). As a result of cross-breeding IRF4$^{Avi\text{-}tag}$ and ROSA26^{BirA} mice, IRF4^{Bio} mice (C57BL/6J-*Irf4*^{em1Bopp} *Gt(ROSA)26*$^{Sortm1.1(birA)Mejr}$) express biotinylated IRF4 due to BirA-mediated *in vivo* biotinylation of the IRF4-Avi-tag fusion protein. IRF4^{Bio} animals were used to conduct IRF4 interactome, proteome as well as IRF4 ChIP-seq experiments. Proteomic analyses of *Irf4*$^{-/-}$ and littermate control animals were performed using CD4^{Cre}xIRF4$^{fl/fl}$ mice, which were generated by crossing CD4^{Cre}[73] with IRF4$^{fl/fl}$ animals.[64]

All animals are based on C57BL/6J background and were bred and housed at the Translational Animal Research Center (TARC) of the Johannes Gutenberg University of Mainz (Mainz, Germany) according to institutionally approved protocols. Animal experiments were performed under the supervision of the authorized investigators in accordance with the European Union normative for care and use of experimental animals with all relevant ethical regulations.

Isolation of murine splenocytes, naïve CD4$^+$ T cells and CD4^{Th17}/CD4^{iTreg} differentiation

In order to obtain splenocytes as well as naïve CD4$^+$ T cells, mice were sacrificed by CO_2 asphyxiation. Afterwards, spleens of IRF4^{Bio} and ROSA26^{BirA} (control) mice were isolated, mechanically disrupted, and filtered from cell debris through a 40-μm cell strainer resulting in splenic single-cell suspensions.

Naïve CD4$^+$ T cells were isolated from splenic single-cell suspensions by negative selecting magnetic-activated cell sorting (MACS) using the Naïve CD4$^+$ T Cell Isolation Kit (mouse, Miltenyi Biotec) according to the manufacturer's protocol. In brief, cells were centrifuged and cell pellets resuspended in GM-buffer (0.5 % (w/v) bovine serum albumin (BSA), 5 mM EDTA in phosphate-buffered saline (PBS), pH 7.3). After addition of the biotin-conjugated monoclonal antibody cocktail provided in the Naïve CD4$^+$ T Cell Isolation Kit, cells were incubated at 4 °C for 5 min. Afterwards, cells were further diluted with GM-buffer and anti-biotin microbeads as well as anti-CD44 microbeads were added to the samples, followed by incubation for 10 min at 4 °C. Magnetic cell separation was performed using LS columns (Miltenyi Biotec). After column equilibration, up to 1 x 10^8 cells were loaded per column and columns were washed twice with GM-Buffer. The flow-through, containing unlabeled naïve CD4$^+$ cells, was collected and centrifuged at 630 xg for 10 min at 4 °C. After centrifugation, naïve CD4$^+$ cells were reconstituted in 10 % (v/v) FCS, 1 % (w/v) sodium pyruvate, 1 % (w/v) glutamine in Iscove's Modified Dulbecco's Medium (IMDM, PAN Biotech), pH 7.2 and transferred to 24-well cell culture plates, which were coated with anti-CD3 and anti-CD28 antibodies as described before.[74] In total, 1 x 10^6 cells were seeded per well. After the addition of polarizing cytokines, cells were cultured for 72 h at 37 °C in a 5 % CO_2 environment. Th17 cell differentiation was induced adding 1 ng/mL TGF-ß, 40 ng/mL IL-6, 2.5 μg/mL anti-IFN-γ and 10 μg/mL anti-IL4 to the medium while for iTreg cells 7.5 ng/ml TGF-ß and 250 ng/ml IL2 was added. For each experiment, splenocytes of three mice were pooled prior to isolation of naïve CD4$^+$ T cells (to obtain sufficient material, i.e., 3-5 x10^7 CD4^{Th17}/CD4^{iTreg} cells, after *ex vivo* differentiation for the AP-procedure).

For FLI1 inhibition experiments, naïve CD4$^+$ T cells were polarized under Th17-skewing conditions as described above. Etoposide (Sigma-Aldrich), dissolved in DMSO, was added in the following concentrations to the cells at the start of differentiation (0 h): 50 nM, 100 nM, 200 nM, 500 nM. DMSO without inhibitor served as control. For AHR inhibition experiments, naïve CD4$^+$ T cells were polarized under Th17-skewing conditions as described above. Resveratrol (Selleckchem) and BAY2416964 (Selleckchem), dissolved in

DMSO, were added to the cells 24 h after the start of differentiation at a concentration of 50 μM and 100 nM, respectively. DMSO without inhibitor served as control.

Isolation of human Th17 cells

In order to isolate human Th17 cells, peripheral blood was obtained by venous puncture of multiple sclerosis patients under treatment with natalizumab (n = 4) in accordance with the approval of the local ethics committee (ethics vote n°2019-14758_1).

Further characteristics of the patient cohort with relapsing-remitting multiple sclerosis (RRMS) are listed below:

	Patients (n = 4, Caucasian) Mean or *n* (range or %)
Age [years]	36.4 (22-46)
Female sex	2 (50)
Years since first diagnosis	3.8 (2-6)
EDSS at baseline*	1.75 (0.0-6.0)
Treatment with natalizumab	4 (100)

*EDSS, expanded disability status scale.

Peripheral blood mononuclear cells (PBMCs) were isolated using Ficoll density gradient centrifugation as described by Larochelle et al.[75]. Afterwards, $CD4^+$ T cells were magnetically enriched using the $CD4^+$ T cell Isolation Kit (human, Miltenyi Biotec) according to the manufacturer's instructions. $CD4^+$ MACS isolated cells were subsequently analyzed and sorted with a BD FACSAria™ III Sorter (for more details see also method section).

Cell lines

HEK293 cells were purchased from DSMZ (German Collection of Microorganisms and Cell Cultures GmbH, Braunschweig, Germany, Cat#: ACC-no.305) and tested for mycoplasma contamination in May 2024.

METHOD DETAILS

Antibodies

Antibodies used in the present study are listed along with their identifier in the key resource table. The following paragraph summarizes which antibodies were used for which type of experiment. The following antibodies were used for fluorescence-activated cell sorting (FACS) analysis of murine cells: brilliant violet 711-conjugated rat anti-mouse CD4 (clone GK1.5, BD Biosciences), phycoerythrin-conjugated rat anti-mouse CD62L (clone MEL-14, BioLegend), brilliant violet 605-conjugated rat anti-mouse/human CD44 (clone IM7, BioLegend), allophycocyanin-conjugated rat anti-mouse/human RORγt (clone AFKJS-9, Thermo Fisher Scientific), phycoerythrin-conjugated rat anti-mouse IL-17A (clone eBio17B7, Thermo Fisher Scientific), fluorescein isothiocyanate-conjugated rat anti-mouse CD25 (clone 3C7, BioLegend), phycoerythrin-conjugated rat anti-mouse FOXP3 (clone FJK-16s, eBiosciences), phycoerythrin- and allophycocyanin-conjugated rat IgG2a,κ isotype controls (Thermo Fisher Scientific).

To sort and analyze human Th17 cells by FACS the following antibodies were used: phycoerythrin-conjugated mouse anti-human/rat CD45RO (UCHL1, Thermo Fisher Scientific), phycoerythrin-cyan7-conjugated mouse anti-human MCAM (P1H12, BD Biosciences), fluorescein-5-isothiocyanate-conjugated mouse anti-human CD4 (SK3, BD Biosciences), Alexa Fluor 700 (AF700)-conjugated mouse anti-human CD3 (UCHT1, Biolegend), and Horizon-conjugated mouse anti-human CCR6 (11A9, BD Biosciences) antibodies were used.

Polyclonal rabbit anti-IRF4 (P173), horseradish peroxidase-conjugated anti-rabbit IgG antibodies as well as horseradish peroxidase-conjugated anti-mouse IgG for Western blot analysis were obtained from Cell Signaling Technology. Monoclonal mouse anti-IRF4 (F-4, clone sc-48338) was purchased from Santa Cruz Biotechnology.

For confocal microscopy analysis, the following antibodies were used: monoclonal phycoerythrin-conjugated rat anti-human/mouse IRF4 (clone 3E4, Thermo Fisher Scientific), phycoerythrin-conjugated rat IgG1κ isotype control (BioLegend) and allophycocyanin-conjugated rat anti-mouse/human CD4 (clone GK1.5, Thermo Fisher Scientific).

Flow cytometry

Purity of isolated, naïve $CD4^+$ T and differentiated Th17 ($CD4^{Th17}$)/iTreg ($CD4^{iTreg}$) cells was analyzed by flow cytometry. Flow cytometry data were acquired on a BD FACSCanto flow cytometer and analyzed using FACSDiva (version 6.1.3, BD) as well as the FlowJo (version 10, BD) software packages.

To characterize naïve $CD4^+$ T cells, cells were stained for 15 min at 4 °C with the eBioscience Fixable Viability Dye eFlour780 (Thermo Fisher Scientific) and labeled with antibodies against appropriate cell surface markers including brilliant violet 711-conjugated anti-CD4 (BD Bioscience), phycoerythrin-conjugated anti-CD62L (BioLegend) and brilliant violet 605-conjugated

anti-CD44 (BioLegend). Cells were washed and resuspended in 0.5 % (w/v) BSA, 5 mM EDTA in PBS (GM-buffer) prior to FACS analysis.

Th17 differentiation was characterized by determining RORγt expression and IL-17 production. Cells were re-stimulated for 3 h at 37 °C in a 5 % CO_2 atmosphere with phorbol myristate acetate (PMA), ionomycin and monensin. After re-stimulation, cells were stained with the eBioscience Fixable Viability Dye eFlour780 and brilliant violet 711-conjugated anti-CD4 as described above. For intracellular staining of RORγt and IL-17A, cells were fixed and permeabilized for 30 min at 4 °C using the Fix/Perm Buffer from Thermo Fisher Scientific. Afterwards, cells were stained with allophycocyanin-conjugated anti-RORγt (Thermo Fisher Scientific) and phycoerythrin-conjugated anti-IL-17A (Thermo Fisher Scientific) in Permeabilization Buffer (Thermo Fisher Scientific) for 30 min at 4 °C. Cells were washed and resuspended in 0.5 % (w/v) BSA, 5 mM EDTA in PBS (GM-buffer) prior to FACS analysis.

Treg differentiation was determined by the expression of CD25 (fluorescein isothiocyanate-conjugated anti-CD25, BioLegend) and FOXP3 (phycoerythrin-conjugated anti-FOXP3, eBioscience). Surface (viability, anti-CD4 and anti-CD25) as well as intracellular (anti-FOXP3) staining was performed as described above for Th17 cells.

Flow cytometric collection and handling of human Th17 cells

For flow cytometry, $CD4^+$ MACS isolated cells were stained with the following antibody-mix: phycoerythrin-conjugated anti-CD45RO (ThermoFisher Scientific), phycoerythin-cyan7-conjugated anti-MCAM (BD Biosciences), fluorescein-5-isothiocyanat-conjugated anti-CD4 (BD Biosciences), alexa fluor 700-conjugated anti-CD3 (Biolegend), and Horizon-conjugated anti-CCR6 (BD Biosciences). Cells were analyzed and sorted with a BD FACSAria™ III Sorter using a 70er nozzle.

For each biological replicate, a total number of 30,000 cells ($CD3^+$ $CD4^+$ $CD45RO^+$ $CCR6^+$ $MCAM^+$ Th17 cells as well as a $CCR6^-$ control population) were directly sorted into SDS-lysis buffer resulting in a final concentration of 1.5 % SDS (w/v), 5 mM DTT, 1x protease inhibitor cocktail in water, i.e., PBS. Cells were subsequently incubated for 5 min at 95 °C and cell lysis was further promoted by sonication for 15 min using a Bioruptor Plus (high, 30s/30s ON/OFF cycle, Diagenode). Cell lysates were subjected to proteolytic digest and proteome analysis by mass spectrometry.

Chemical cross-linking and isolation of nuclei

Murine $CD4^{Th17}$/$CD4^{iTreg}$ cells were harvested and washed twice with PBS to remove remaining media. A fresh Dithiobis[succinimidyl propionate] (DSP, Thermo Fisher Scientific) solution (20 mM) in DMSO was prepared for each experiment and further diluted in PBS, pH 8.3 to a final working concentration of 0.75 mM DSP. Cells were cross-linked according to the manufacturer's protocol for 30 min at room temperature. The reaction was stopped by adding Tris (pH 7.5) to a final concentration of 10 mM, followed by incubation for 15 min at room temperature. Afterwards, cells were washed twice with PBS to remove remaining DSP. In order to isolate cell nuclei, cells were resuspended in a hypotonic buffer (20 mM Tris-HCl, 10 mM NaCl, 3 mM $MgCl_2$, pH 7.4). After incubation for 12 min on ice, NP-40 was added to a final concentration of 0.5 % (v/v) to the samples and cells were vortexed for 10 s to disrupt cell membranes. Nuclei were washed twice with PBS and pelleted by centrifugation at 850 xg for 10 min at 4 °C. Isolated nuclei were either stored at -80 °C until further processing or directly subjected to immunoprecipitation.

Isolation of IRF4 complexes

Nuclei were resuspended in Cell Lysis Buffer from the μMACS FactorFinder Kit (Miltenyi Biotec), which was supplemented with proteinase inhibitor cocktail according to manufacturer's instructions (Roche). Nuclear lysis and disruption of DNA was promoted by sonication at 4 °C for 10 min using a Bioruptor Plus (low, 30 s/30 s ON/OFF, Diagenode). After lysis of nuclei, samples were centrifuged for 6 min at 14,850 xg at 4 °C and supernatant containing nuclear proteins was subjected to immunoprecipitation. Streptavidin-coated magnetic beads (Dynabeads™ M-280, Thermo Fisher Scientific) were washed with a mixture of Cell Lysis and Binding Buffer (1:3 (v/v), μMACS FactorFinder Kit, Miltenyi Biotec) for 10 min at room temperature. Afterwards, beads were resuspended in Binding Buffer supplemented with Binding Enhancer (both derived from the μMACS FactorFinder Kit, Miltenyi Biotec) and added to the nuclear lysates. After overnight incubation at 4 °C, samples were incubated for 2 min on a magnetic rack until beads were settled. Supernatant was discarded and samples were washed three times with RIPA buffer (25 mM Tris-HCl, 150 mM NaCl, 1 % (v/v) NP-40, 1 % (w/v) sodium deoxycholate, 0.35 % (w/v) SDS, pH 7.5) for 10 min at room temperature. Afterwards, the samples were washed three times with 25 mM Tris (pH 7.5) for 10 min at room temperature. Proteins were eluted incubating the streptavidin-coated beads in an SDS/biotin-containing buffer (1 % (w/v) SDS, 10 mM biotin, 10 mM Tris pH 7.5) for 5 min at 95 °C.

Proteolytic digestion

Proteins released from IRF4 pulldown experiments as well as murine $CD4^{Th17}$/$CD4^{iTreg}$ and human Th17 (and $CCR6^-$) cell lysates were processed by single-pot solid-phase-enhanced sample preparation (SP3) as detailed before with minor modifications[76,77]: In case of IRF4 pulldown experiments, proteins and DSP cross-linker were reduced with 45 mM DTT for 30 min at 37 °C. Afterwards, temperature was increased to 45 °C and samples were incubated for another 10 minutes. Whole cellular lysates were incubated with 20 mM DTT for 30 min at 45 °C. In all cases (IRF4 pulldown and sample preparation of murine $CD4^{Th17}$/$CD4^{iTreg}$ cells), proteins were alkylated for 30 min at room temperature using iodoacetamide (IAA). Excess IAA was quenched by the addition of DTT. Afterwards, 2 μL of carboxylate-modified paramagnetic beads (Sera-Mag SpeedBeads, GE Healthcare, 0.5 μg solids/μL in water as described by Hughes et al.[77]) were added to the samples. After adding acetonitrile to a final concentration of 70 % (v/v), samples were allowed to

settle at room temperature for 20 min. Samples were mixed after 10 min. Subsequently, beads were immobilized by incubation on a magnetic rack for 2 min and washed twice with 70 % (v/v) ethanol in water and once with acetonitrile. Beads were resuspended in 50 mM NH_4HCO_3 supplemented with trypsin (Mass Spectrometry Grade, Promega) at an enzyme-to-protein ratio of 1:25 (w/w) and incubated overnight at 37 °C. After overnight digestion, acetonitrile was added to the samples to reach a final concentration of 95 % (v/v). Subsequently, samples were incubated for 20 min at room temperature (and mixed after 10 min). To increase the yield, supernatants derived from this initial peptide-binding step were additionally subjected to the SP3 peptide purification procedure as described before.[76] Each sample was washed with acetonitrile. To recover bound peptides, paramagnetic beads from the original sample and corresponding supernatants were pooled in 2 % (v/v) dimethyl sulfoxide (DMSO) in water and sonicated for 1 min. After 2 min of centrifugation at 16,200xg and 4 °C, supernatants containing tryptic peptides were transferred into a glass vial for MS analysis and acidified with 0.1 % (v/v) formic acid.

Western blot analysis

Protein samples were separated via SDS-Polyacrylamide Gel Electrophoresis (SDS-PAGE). After electrophoretic separation, proteins were transferred onto a PVFD membrane (0.45 μm pore size, GE Healthcare). The membrane was blocked with 5 % (w/v) BSA in TBS-T buffer (1 mM Tris-base, 9 mM Tris-HCl, 150 mM NaCl, 1 % (v/v) Tween in H_2O) for 1 h, followed by incubation with a primary polyclonal rabbit anti-IRF4 antibody (P173, Cell Signaling Technology, 1:1,000) overnight. A secondary horseradish peroxidase–conjugated anti-rabbit IgG (Cell Signaling Technology, 1:2,000) was used for detection. Biotinylated proteins were detected using a horseradish peroxidase–conjugated streptavidin (Roche, 1:1,000) and visualized using WesternBright Chemiluminescence substrates (Biozym). The chemiluminescence signal was captured with a Bio-Rad ChemiDoc XRS imager and analyzed using the Quantity One software (version 4.4.0, Bio-Rad).

Liquid chromatography-mass spectrometry (LC-MS) analysis

LC-MS analyses from initial AP experiments during protocol optimization (i.e., splenocytes) were conducted on a nanoAcquity UPLC system (Waters Corporation), which was coupled online to a Synapt G2-S HDMS mass spectrometer (Waters Corporation) via a NanoLockSpray dual electrospray ion source (Waters Corporation). Tryptic digests were loaded onto an HSS-T3 C18 1.8 μm, 75 μm x 250 analytical reversed-phase column (Waters Corporation) in direct injection mode as described before.[78] Mobile phase A was water containing 0.1 % v/v formic acid and 3 % (v/v) DMSO, while mobile phase B was ACN containing 0.1 % v/v formic acid and 3 % (v/v) DMSO in ACN.[79] Peptides were separated running a gradient of 5–40 % mobile phase B over 90 min at a flow rate of 300 nL/min. Afterwards, the column was rinsed for 5 min with 90 % mobile phase B, followed by a re-equilibration step at initial conditions resulting in a total analysis time of 120 min. The column temperature was maintained at 55 °C. MS analysis of eluting peptides was performed by ion-mobility separation (IMS) enhanced data-independent acquisition (DIA) in $UDMS^E$ mode as detailed before.[78,80]

LC-MS analyses of the murine $CD4^{Th17}$/$CD4^{iTreg}$ IRF4 interactome as well as the murine $CD4^{Th17}$/$CD4^{iTreg}$ and human Th17 cell proteome were performed on an Ultimate 3000 RSLCnano LC system (Thermo Fisher Scientific) coupled to an Orbitrap Exploris 480 instrument platform (Thermo Fisher Scientific). Tryptic peptides were first loaded onto a PEPMAP100 C18 5 μm 0.3 x 5 mm trap column (Thermo Fisher Scientific) and subsequently separated on an HSS-T3 C18 1.8 μm, 75 μm x 250 mm analytical reversed-phase column (Waters Corporation). Mobile phase A was water containing 0.1 % (v/v) formic acid and 3 % (v/v) DMSO. Peptides were separated running a gradient of 2–35 % mobile phase B (0.1 % (v/v) formic acid, 3 % (v/v) DMSO in ACN) over 40 min at a flow rate of 300 nL/min. Total analysis time was 60 min including wash and column re-equilibration steps. Column temperature was set to 55 °C. The following settings were used for mass spectrometric analysis of eluting peptides on the Orbitrap Exploris 480 instrument platform: Spray voltage was set to 1.8 kV, the funnel RF level to 40, and heated capillary temperature was at 275 °C. Data were acquired in DIA mode. Full MS resolution was set to 120,000 at *m/z* 200 and full MS automated gain control (AGC) target to 300 % with a maximum injection time (IT) of 20 ms. Mass range was set to *m/z* 345 – 1250. Fragment ion spectra were acquired with an AGC target value of 1000 %. In total, 20 windows with varying sizes (adjusted to precursor density) were used with an overlap of 0.5 Th. Resolution was set to 30,000 and IT was determined automatically (“auto mode”). Normalized collision energy was fixed at 27 %. All data were acquired in profile mode using positive polarity.

For the analysis of the IRF4 knock-out (*Irf4*$^{-/-}$) data set, reconstituted peptides were injected and separated on a nanoElute LC system (Bruker Corporation, Billerica, MA, USA) at 400 nL/min using a reversed phase C18 column (Aurora UHPLC emitter column, 25 cm x 75 μm 1.6 μm, IonOpticks) which was heated to 50°C. Peptides were loaded onto the column in direct injection mode at 600 bar. Mobile phase A was 0.1% FA (v/v) in water and mobile phase B 0.1% FA (v/v) in ACN. Peptides were separated running a linear gradient from 2% to 37% mobile phase B over 39 min. Afterwards, column was rinsed for 5 min at 95% B. Eluting peptides were analyzed in positive mode ESI-MS using parallel accumulation serial fragmentation (PASEF) enhanced DIA mode[81] on a timsTOF Pro 2 mass spectrometer (Bruker Corporation). The dual TIMS (trapped ion mobility spectrometer) was operated at a fixed duty cycle close to 100% using equal accumulation and ramp times of 100 ms each spanning a mobility range from $1/K_0$ = 0.6 Vs cm^{-2} to 1.6 Vs cm^{-2}. We defined 36 × 25 Th isolation windows from *m/z* 300 to 1,165 resulting in 15 diaPASEF scans per acquisition cycle. The collision energy was ramped linearly as a function of the mobility from 59 eV at $1/K_0$ = 1.3 Vs cm^{-2} to 20 eV at $1/K_0$ = 0.85 Vs cm^{-2}.

All samples were analyzed in three technical replicates.

Chromatin immunoprecipitation coupled with sequencing (ChIP-seq)

For ChIP-seq experiments 1 – 1.5 x 10^7 differentiated Th17 ($CD4^{Th17}$) or iTreg ($CD4^{iTreg}$) cells were washed twice with medium containing 5 % (v/v) FCS, 1 % (w/v) sodium pyruvate, 1 % (w/v) glutamine in Iscove's Modified Dulbecco's Medium (IMDM, PAN Biotech), pH 7.2. The cells were fixed with a final concentration of 1 % formaldehyde (Pierce 16 % formaldehyde, methanol-free, ThermoFisher) for 7 min at room temperature. To quench the reaction a final concentration of 125 mM of glycerin was added to the solution for 5 min at room temperature. During the fixing and quenching procedure, the samples were inverted from time to time. To remove remaining medium components, the cells were washed twice with cold PBS and were transferred into TPX microtubes (Diagenode). The dry cell pellet was stored over night at –80 °C. Before adding the lysis buffer (50 mM Tris pH 7.9, 10 mM EDTA pH 8, 1 % (w/v) SDS in nuclease-free water, QIAGEN) supplemented with proteinase inhibitor cocktail (Roche), the cell pellet was scratched over a rack to loosen it. The lysis buffer was incubated at least for 30 min on ice followed by the sheering of the cells 6 times with a 1 mL syringe through a 21G x $1^{1/2}$ '' 0.8 x 40 mm needle on ice. To fragment the chromatin for an average size of 200-500 bp, the cells were sonicated 3-6 times (cycles) at 4 °C each for 10 min using the Bioruptor Plus (high, 30 s/30 s ON/OFF, Diagenode). Between every cycle, the cells were inverted and quickly spun down. The supernatant was collected in a new 1.5 mL tube after centrifugation 15 min at 17,000 xg, 4 °C. Afterwards the DNA content was determined and adjusted between the $IRF4^{Bio}$ and $ROSA26^{BirA}$ (control) sample. Streptavidin-coated magnetic beads (Dynabeads™ M-280, Thermo Fisher Scientific) were equilibrated with 80 % (v/v) IP buffer (30 mM Tris pH 7.9, 2 mM EDTA pH 8, 165 mM NaCl, 0.3 % (w/v) SDS, 1 % (v/v) Triton X-100 in nuclease-free water) and 20 % (v/v) of lysis buffer by rolling for 5-10 min at room temperature. IP buffer was added to the sample to gain a 4:1 ratio of IP:lysis buffer. A small amount of sample was removed serving as an input control in the real-time PCR after chromatin immunoprecipitation. The washed streptavidin-coated magnetic beads were added to the sample and incubated rolling for 4 h at room temperature before overnight incubation at 4 °C. The beads were washed once with IP buffer supplemented with proteinase inhibitor cocktail rolling 30 min at room temperature. After the beads settled on a magnetic rack the supernatant was discarded. Further washing steps followed, each step rolling for 30 min at room temperature and supplemented with proteinase inhibitor cocktail: twice with a washing buffer containing 2 % SDS (in nuclease-free water), twice with a washing buffer containing 10 mM Tris pH 7.9, 1 mM EDTA pH 8, 250 mM LiCl, 1 % (v/v) NP-40, 1 % (v/v) sodium deoxycholate (in nuclease-free water) and twice with a washing buffer containing 20 mM Tris pH 7.9, 1 mM ETDA pH 8, 50 mM EDTA, 0.1 % (v/v) SDS (in nucleas-free water). Before the addition of the elution buffer (10 mM Tris pH 7.9, 5 mM EDTA pH 8.0, 1 % (w/v) SDS, 500 mM NaCl in nuclease-free water), a 15 min washing step at room temperature only with nuclease-free water was included. For the treatment with RNaseA and proteinase K, the input control from the previous day was included and to all samples 50 μg/mL RNaseA (DNase and protease-free, ThemoFisher) was added to all samples. Samples were then incubated for 1 h at 37 °C. Afterwards, 150 μg/mL proteinase K (from *Tritirachium album*, Serva) was added and samples were incubated 90 min at 42 °C. All samples were incubating rolling at 65 °C overnight. The DNA Clean & Concentrator Kit (Zymo Research) was used to clean and concentrate the chromatin fragments according to the manufacturer's protocol. Before the samples were sent for sequencing the fold enrichment of the immunoprecipitated chromatin was calculated using a real-time PCR. For that a target region, where IRF4 binds (*Il10*, fwd: 5'AATCC GAGAAACCCACCA3', rev: 5' TCCATACCAAAACCCCAG3') as well as an off-target region, where IRF4 does not bind (Ezh2, fwd: 5'CTTCTCAACCCCTTTCCCTAAGA3', rev: 5'CACCTTATTCCCAAAGGCAAGG3') were selected. All samples with an at least 4-fold enrichment were used to generate a DNA library. For this the NEBNext Ultra II DNA Library Prep Kit for Illumina (New England BioLabs) was used according to the recommended protocol for low input material.

Immunostaining for confocal fluorescence microscopy

Between 5x10^5 to 1.5x10^6 cells were used per preparation. After harvest, cells were washed twice with PBS or PBS supplemented with 0.5 % (w/v) BSA and 5 mM EDTA and subjected to immunostaining. Cells were first incubated with an allophycocyanin-conjugated anti-CD4 antibody (Thermo Fisher Scientific, 1:500 dilution) in PBS for 20 min at 4 °C. Afterwards, the cells were washed twice with PBS. Cells were subsequently fixed and permeabilized for 30 min at 4 °C using Fix/Perm Buffer (Thermo Fisher Scientific). Afterwards, cells were washed twice with Permeabilization Buffer (Thermo Fisher Scientific) and cells were incubated with phycoerythrin-conjugated anti-IRF4 antibody (Thermo Fisher Scientific, 1:500 dilution) in PBS for 30 min at 4 °C. After washing cells twice with PBS, cells were incubated with Hoechst (ImmunoChemistry Technologies, 1:500 dilution) in PBS for 5 min at 4 °C. Afterwards, cells were washed twice with PBS and resuspended in 40 μL of warm (37 °C) Mowiol (produced in-house). Reconstituted cells were then transferred onto a glass slide (Diagonal), covered with a no.1.5H cover glass (Paul Marienfeld GmbH) and samples were allowed to dry for 6 to 12 h at room temperature prior to storage at 4 °C and/or imaging at the confocal microscope.

Confocal microscopy

The fixed and stained cells were imaged on a Leica TCS SP8 confocal microscope with either a 20X 0.75 NA air objective or with a 63X 1.40 oil immersion objective sequentially with exposure to a 405 nm laser for transmission images and for Hoechst excitation with emission and detection within a spectral window of 440 nm to 480 nm, with 552 nm laser exposure for phycoerythrin excitation and with emission and detection within a spectral window of 565 nm to 625 nm and with 638 nm laser exposure for allophycocyanin excitation with emission and detection within a spectral window of 650 nm to 735 nm. The images were always acquired using Imaris version 9.3.1 (BitPlane) at a factor of 2.3 times greater than the calculated confocal spatial lateral resolution, at a scan rate of 200 lines/second and with 4x averaging. All images used in comparison were prepared and acquired under the same conditions.

The images shown in the figures were smoothed with the standard Leica smoothing algorithm. In some cases, the Hoechst signal was processed by having the upper threshold lowered by up to 20 % in order to create homogenous nuclear images and homogenous cell nuclear borders. In some cases, the CD4 allophycocyanin signal had up to a 10 % cutoff and/or a 10 % threshold applied in order to create a homogeneous cell border. The IRF4 phycoerythrin signal intensity was left unchanged.

Plasmid construction

The donor and acceptor vectors pcDNA3.1-cmyc-NL-GW (Addgene plasmid ID #113446), pcDNA3.1-GW-NL-cmyc (Addgene plasmid ID #113447), pcDNA3.1, pcDNA3.1-cmyc-NL (Addgene plasmid ID #113442), and pcDNA3.1-PA-mCit (Addgene plasmid ID #113443) were kindly provided by the Wanker Group (Max-Delbrück-Centrum für Molekulare Medizin, Germany). Plasmids pcDNA3.1-GW-His3C-mCit and pcDNA3.1-mCit-His3C-GW were generated in house by introducing a Protease 3C cleavage site between the GATEWAY cassette and mCitrine starting off from plasmids pcDNA3.1-mCit-GW and psDNA3.1-GW-mCit provided by the Wanker lab. By default, we cloned all ORFs of interest into *N*- and *C*-terminal NL and mCit fusion destination vectors. Trepte et al. showed that testing protein pairs in different configurations increases detection rates while maintaining low false positive rates because BRET signals are higher if fusions are close to the actual interaction interface.[50] Human open reading frames (ORFs) in GATEWAY entry vectors were obtained from an in-house ORFeome collection in form of bacterial glycerol stocks.[82] The glycerol stock was scraped and material used to inoculate in 96-well plates (Corning), with each well containing 200 μL of LB medium and antibiotics. The plate was incubated at 37 °C and left to shake overnight at 190 rpm. In a 96-well PCR plate (Starlab) 4 μL of bacteria culture was used per 50 μL PCR reaction (denaturation at 98 °C for 10 s, annealing at 55 °C for 30 s and extension at 72 °C for 3 min, 30 cycles of amplification) using phusion high-fidelity polymerase (NEB) and primers annealing to the backbone of the plasmid (forward: 5′TTGTAAAACGACGGCCAGTC and reverse: 5′ GCCAGGAAACAGCTATGACC) to amplify the insert and flanking GATEWAY att sites. Proper insert amplification was confirmed via agarose gel electrophoresis using 6 μL per well. In a 96-well PCR plate 1 μL of each amplified PCR product together with 200 ng of above-mentioned destination vectors were directly used per 10 μL LR reaction using 4x LR clonase (Invitrogen) to generate expression vectors. After Proteinase K digestion (2 μg/well) for 10min at 37°C, the full 10 μL of LR reaction was transformed into chemically competent DH5a cells (30 μl) in a 96-well PCR plate, then recovered in 80 μL of pre-warmed SOC medium at 37 °C for 1 h without shaking. 70 μL of transformed bacteria was plated in each well of 48-well square agar plates and incubated at 37 °C overnight. Colonies were picked and inoculated into a 96 deep-well plate containing 2 ml of LB medium and 100 μg/mL ampicillin. The plate was incubated at 37 °C with continuous shaking at 700 rpm in the incumixer for 24 h. The plasmids were extracted from the inoculated culture using a Plasmid Plus 96-well Miniprep kit (Qiagen). The concentration of each purified DNA solution was determined with a Nanophotometer and diluted to 100 ng/μL. 600 ng of each DNA solution was used for Sanger sequencing using the backbone primers (forward: GGCTAACTAGAGAACCCACTG and reverse: GGCAACTA GAAGGCACAGTC, the tag-specific NanoLuc forward: 5′GAACGGCAACAAAATTATCGAC and reverse: CCCCGAGATTCTGA AACAAAC, mCitrine forward: 5′AGCAGAATACGCCCATCG and reverse: 5′ AGTGTGAGTTTCCCATATGTCG). The ORFs BACH2 (pcDNA3.1 BACH2-NL-cmyc, pcDNA3.1 mCit-His3C-BACH2, pcDNA3.1 BACH2-His3C-mCit), HMMR (pcDNA3.1 mCit-His3C-HMMR, pcDNA3.1 HMMR-His3c-mCit, pcDNA3.1 HMMR-NL-cmyc, pcDNA3.1 cmyc-NL-HMMR), RNF40 (pcDNA3.1 mCit-His3C-RNF40, pcDNA3.1 RNF40-His3c-mCit, pcDNA3.1 RNF40-NL-cmyc, pcDNA3.1 cmyc-NL-RNF40) and SATB1 (pcDNA3.1 mCit-His3C-SATB1, pcDNA3.1 SATB1-His3c-mCit, pcDNA3.1 SATB1-NL-cmyc) due to their length were only partially covered by reads from both ends. Mutations deemed non-deleterious were identified in plasmids pcDNA3.1 cmyc-NL-GIPC2 and pcDNA3.1 SPI1-His3C-mCit. All ORF sequences used in this study are available in Table S11.

BRET assay

HEK293 cells were grown and maintained in high-glucose (4.5 g/l) DMEM (Thermo Fisher) for BRET assays. Media was supplemented with 10% fetal bovine serum (Thermo Fisher) and 1% Penicillin/Streptomycin. Cells were grown at 37 °C, 5% CO_2, and 85% RH. Cells were subcultured every 2–3 days and transfected with lipofectamine 2000 transfection reagent (Invitrogen) in Opti-MEM medium (Thermo Fisher) using the reverse transfection method according to the manufacturer's instructions. For transfections, cells were seeded at a density of 4.0×10^4 cells per well in a white 96-well microtiter plate (Greiner) in phenol-red-free, high-glucose DMEM media (Thermo Fisher) supplemented with 5% fetal bovine serum (Thermo Fisher). Transfections were performed with a total DNA amount of 200 ng per well. If the expression plasmid concentration amount was below 200 ng/well, pcDNA3.1 (+) was used as a carrier DNA to reach the total amount of DNA of 200 ng. The protein pairs were tested in both N- and C-terminal fusion orientations, 8 combinations in total, depending on plasmid cloning success (NL-A with mCit-B, NL-B with mCit-A, A-NL with B-mCit and B-NL with A-mCit, NL-A with B-mCit, NL-B with A-mCit, A-NL with mCit-B, B-NL with mCit-A). The plate with transfected cells was incubated 2 days at 37 °C, 5% CO_2, and 85% RH before measurements. All measurements were done with the Infinite M200 Pro microplate reader (Tecan). First, 100 μL of the medium was aspirated from each well. The mCitrine fluorescence (FL) was measured in intact cells (excitation/emission 513 nm/548 nm) using a gain of 100 with four measurements per well that were averaged to estimate expression levels of mCit fusion proteins. After measuring the fluorescence, coelenterazine-h (PJK Biotech GmbH) was added to a final concentration of 5 μM. The cells were briefly shaken for 15 s and incubated for 15 min inside the plate reader at 37 °C. After incubation, total luminescence was measured over an integration time of 1 s to estimate expression levels of NL fusion proteins. Subsequently, the BRET was determined by measuring over a short-wavelength (WL) and long-wavelength range the luminescence using the dual filters BLUE1 (370–480 nm) and the GREEN1 (520–570 nm) at 1000 ms integration time. The BRET is the ratio of

luminescence from the long over the short wavelength measurement. Corrected BRET ratios were calculated as described in Trepte et al.[50]. Briefly, for every transfected protein pair NL-A and mCit-B, the following two control pairs were measured: NL-Stop with mCit-B and NL-A with mCit-Stop. The maximal BRET from both control pairs was subtracted from the actual test pair to correct for donor bleedthrough, unspecific binding to the tags, and background signal. To determine whether a protein pair interacted in the BRET assay or not, we used donor:acceptor DNA transfection ratios of 2:50 ng. We requested that cBRETs determined at these transfection ratios were $\geq$0.04.

QUANTIFICATION AND STATISTICAL ANALYSIS

Analysis of mass spectrometric data and label-free quantification

Processing and database search of the Synapt G2-S raw data were performed using ProteinLynx Global SERVER (PLGS, version 3.0.2, Waters Corporation). Data were searched against a custom compiled database containing UniProtKB/SwissProt entries of the mouse reference proteome (UniProtKB release 2020_03, 17,033 entries) and a list of common contaminants as described before.[78] Postprocessing of data including retention time alignment, EMRT (exact mass retention time) and IMS clustering, as well as protein homology filtering was conducted using the software tool ISOQuant (ver.1.8) as detailed before.[78,80] Each pulldown experiment was processed separately. An experiment-wide FDR of 0.01 was applied at the peptide-level for cluster annotation in ISOQuant. Moreover, only proteins that had been identified by at least two peptides with a minimum length of 7 amino acids, a minimum PLGS score of 6.0 and no missed cleavages were considered for quantitative analysis in the final dataset. For each protein absolute in-sample amounts were calculated using TOP3 quantification as described before.[83] IRF4 interacting proteins had to show a 2-fold enrichment as compared to the controls.

DIA raw data acquired with the Exploris 480 and the timsTOF Pro2 platforms were processed using DIA-NN (version 1.7.13)[67] applying the default parameters for library-free database search. Murine data were searched using a custom compiled database containing UniProtKB/SwissProt entries of the murine reference proteome (UniProtKB release 2021_04, 17,068 entries) and a list of common contaminants, and human Th17 data against a custom compiled database containing UniprotKB/Swissprot entries of the human reference proteome (UniProtKB release 2020_03, 20,365 entries) and a list of common contaminants. For peptide identification and *in-silico* library generation, trypsin was set as protease allowing one missed cleavage. Carbamidomethylation was set as fixed modification and the maximum number of variable modifications was set to zero. The peptide length ranged between 7–30 amino acids. The precursor *m/z* range was set to 300–1,800, and the product ion *m/z* range to 200–1,800. As quantification strategy we applied the ''any LC (high accuracy)'' mode with RT-dependent median-based cross-run normalization enabled. We used the build-in algorithm of DIA-NN to automatically optimize MS2 and MS1 mass accuracies and scan window size. Peptide precursor FDRs were controlled below 1 %. In the final proteome datasets, proteins had to be identified by at least two peptides and had to be present in at least eight runs in at least one of the conditions. In the proteome analysis of $CD4^{Th17}$/$CD4^{iTreg}$ cells from *Irf4*$^{-/-}$ and littermate controls, the run filter was set to at least seven runs out of twelve in at least one condition. The final IRF4 interactome dataset was filtered to only contain proteins identified by more than two peptides and present in at least eight out of nine runs in at least one of the conditions. Additionally, the cross-run normalization was disabled.

Statistical analysis of proteomic and FACS datasets

Statistical analysis of murine proteomic datasets was conducted with the limma package.[84] For the interactome data, proteins, identified in at least eight out of nine LC-MS runs in the $IRF4^{Bio}$ condition, with an adjusted *p*-value of 0.01 and a $\log_2$-fold change ($IRF4^{Bio}$/Ctrl) larger than 1 were considered as significantly enriched. In case of the proteomic datasets, proteins with an adjusted *p*-value of 0.01 and a $\log_2$-fold change either below -0.5 or above 0.5 were considered significant differentially expressed.

To enable limma to work with the intensities, they were log transformed. We utilized DEPs mixed imputation method to impute missing data differently for missing at random (MAR) and missing not at random (MNAR) data: MNAR values were imputed with the minimum value present in the data, while MAR values were imputed with K-Nearest Neighbor imputation, both as implemented in the DEP package.[85] Despite limma's capabilities of working with data with missing values, we favored imputation as some of the most interesting proteins, would be those that could not be identified or could not pass the detection threshold in the control, but would do so in the $IRF4^{Bio}$ data. For the proteome, in both cell types compared, proteins that passed the threshold in only one of the groups would be of interest.

The design for limma's linear model was different for the proteome and the interactome analysis, respectively: For the proteome analysis just the cell type, which was the comparison of interest, was given to the model as factor. In the interactome analysis, additional to the comparison of interest, which was the control mice against the $IRF4^{Bio}$ mice, we added the experiments as a co-factor. This was done to counteract the bias of an outlier experiment, which had generally lower intensities than its partner experiments.

Principal component analysis was conducted for plotting using the package FactoMineR[86] and heatmaps were plotted with pheatmap.[87] ggplot2 was used for scatterplots.[88] Differential proteins or clusters in heatmaps were annotated with the GO terms with the clusterprofiler package.[89]

Statistical analysis of the proteomic data from the analysis of human Th17 cells and respective $CCR6^-$ control populations was conducted using Student's t-test, which was corrected by the Benjamini-Hochberg (BH) method for multiple hypothesis testing (FDR of 0.01).

Cell differentiation data obtained from FACS analysis of etoposide treated and non-treated control cells (i.e., percentage of IL-17$^+$ cells) was plotted and statistically analyzed using GraphPad Prism (version 10.3.1). To test for significant differences between the control (w/o) and the etoposide treated (100 nM) group a two-tailed Welch's t-test was conducted in GraphPad Prism.

Functional annotation and downstream data analysis

Functional annotation analysis was performed using GO terms powered by PANTHER (version 14.0)[68] (http://geneontology.org/). Network analysis was conducted using the STRING database (version 11.0)[70] through its web interface as well as the stringApp[90] in Cytoscape (version 3.8.0).[69] Protein networks in STRING were generated using default settings. Venn diagram data were calculated using the Venny web application (http://bioinfogp.cnb.csic.es/tools/venny/index.html).

Data analysis of sequencing data (ChIP-Seq)

We used seqQscorer[65] for quality control of the raw data. For the downstream analysis of the sequencing data, the software EaSeq (version 1.2, https://easeq.net)[66] was used to call peaks. As a reference, the mm10 genome was used. For peak calling in CD4^{Th17} cells the following parameters were used: window size: 100 bp, FDR: 1x10^{-15}, p-value: 1x10^{-20}, log$_2$: 2.1 and merge distance: 0 bp. For CD4^{iTreg} cells the parameters were adjusted to: window size: 100 bp, FDR: 1x10^{-10}, p-value: 1x10^{-10}, log$_2$: 1.5 and merge distance: 100 bp. The peaks were annotated to the nearest start or end of a gene (annotation "Start&End"). ChIPseeker[71] was used to additionally annotate called peaks.

To search for enrichment in enhancer and silencer regions, we conducted a search in the silencers found in mouse blood according to silencerDB[42] and the enhancers provided in the EnhancerAtlas 2.0[41] and filtered for CD4$^+$ cells as a source. As both these databases were using mm9 we used UCSCs LiftOver (https://genome.ucsc.edu/cgi-bin/hgLiftOver) to remap them to mm10. We used ChIPPeakAnno[72] to search for an overlap between the two respective databases and the peaks of both CD4^{Th17} and Treg cells. To ensure the found overlap is not random we conducted a random permutation test with 1,100 iterations as implemented in ChIPPeakAnno.

Ab initio motif enrichment analysis of the IRF4 ChIP-Seq peaks derived from CD4^{Th17} and CD4^{iTreg} cells was executed using the MEME suite with default parameters.[46] Identified motifs were annotated using Tomtom[47] with a similarity threshold of 0.05, in conjunction with the position-specific scoring matrices (PSSM) of murine TFs from the TRANSFAC database.[44]

To enhance motif annotation, we additionally employed the MATCH algorithm[43] annotating known TF binding sites. This process incorporated PSSMs corresponding to CD4^{Th17} and CD4^{iTreg} interactors, as well as the profile of immune-specific TFs as defined by TRANSFAC.[44] We established a stringent cutoff threshold, accepting motif annotations only if they matched both the core sequence and matrix sequence of PSSMs with a similarity score of 0.8 or higher.

To further investigate the combinatorial activity of TFs, we quantified the number of peaks bound by two distinct TF motifs within a spatial proximity of equal or less than five base pairs. This approach facilitated a detailed exploration into the complex interplay of TFs within CD4^{Th17} and CD4^{iTreg} cells.

Public ChIP-Seq datasets for comparison with our dataset were reanalyzed with the same workflow as described above. The following public ChIP-Seq datasets were used for the comparison with the data from the present study: SRR10092114, SRR10092116, SRR10092118, SRR10092120, SRR1199226, SRR18458264, SRR18458265, SRR18458266, SRR18458270, SRR18458271, SRR18458272, SRR571609, SRR571610, and SRR571611.